



**Emerging Interface Materials for Electronics Thermal
Management: Experiments, Modeling, and New
Opportunities**

Journal:	<i>Journal of Materials Chemistry C</i>
Manuscript ID	TC-REV-10-2019-005415.R1
Article Type:	Review Article
Date Submitted by the Author:	04-Dec-2019
Complete List of Authors:	Cui, Ying; University of California Los Angeles, School of Engineering and Applied Science Li, Man; University of California Los Angeles, School of Engineering and Applied Science Hu, Yongjie; University of California Los Angeles, School of Engineering and Applied Science

ARTICLE

Emerging interface materials for electronics thermal management: experiments, modeling, and new opportunities

Received 00th January 20xx,
Accepted 00th January 20xx

Ying Cui†, Man Li†, Yongjie Hu*

DOI: 10.1039/x0xx00000x

Thermal management is becoming a critical technology challenge for modern electronics with the decreasing device size and increasing power density. One key materials innovation is to develop advanced thermal interfaces in electronic packaging to enable efficient heat dissipation and improve device performance, which has attracted intensive research efforts from both academia and industry during last several decades. Here we review the recent progress in both theory and experiment for developing high-performance thermal interface materials. First, the basic theories and computational frameworks for interface energy transport are discussed, ranging from atomistic interface scattering to multiscale disorders that contributed to thermal boundary resistance. Second, state-of-the-art experimental techniques including steady-state and transient thermal measurements are discussed and compared. Moreover, the important structure design, requirement, and property factors for thermal interface materials depending on different applications are summarized and exemplified with recent literature. Finally, emerging new semiconductors and polymers with high thermal conductivity are briefly reviewed and opportunities for future research are discussed.

1. Introduction

With the decreasing size and increasing power densities of modern electronics, heat dissipation is becoming one of the most critical technological challenges¹⁻⁷. A key part of thermal management is to enhance the heat transfer between heterogeneous materials interfaces, which is critical to the overall thermal performance of nanoscale devices⁸⁻¹³. For example, in typical microprocessors packaging (Figure 1), heat generated from the chip is expected to be dissipated to the heat spreader and to the heat sink, however through a multilayer device structure. At each interface, an additional thermal boundary resistance (TBR)¹⁻⁴ exists to impede heat dissipation. In addition, the electronic performance and device lifetime can degrade dramatically under continuous overheating and large thermal stress at the interfaces. Therefore, for last several decades, there have been intensive efforts in developing advanced thermal interface materials (TIMs) in the aim to minimize the TBR between layers and enhance thermal management performance, as well as tackling application requirements such as low thermal stress between materials of different thermal expansion coefficients, low elastic modulus or viscosity, flexibility, and reusability.

This review focuses on the transport mechanisms and materials aspects of TIMs. We begin by introducing the basic theories of interface thermal transport based on atomistic scattering to the lumped TBR contributed by multiple factors at practical materials interfaces. Then we describe state-of-

the-art experimental techniques for thermal measurement and characterizations. We further summarize recent progress in the material design of TIMs including fillers, matrixes, and structural optimization. In addition, emerging new high thermal conductivity materials including boron arsenide, boron phosphide, and conducting polymers are highlighted to show the potential in developing advanced TIMs. Key achievements, challenges, and the future opportunities in this field are discussed.

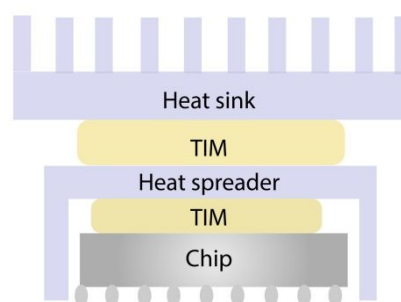


Fig. 1 Thermal interface materials (TIMs) and thermal boundary resistance (TBR) in microchip packaging. Typical electronics packaging using TIM to improve TBR and heat dissipation from the chip to heat sink.

2. Basic theory and mechanism for interface energy transport

TIMs are functional materials for addressing heat dissipation issues brought by the TBR at a junction between two components. TBR has become one of the main technological bottlenecks in modern electronics and is responsible for the

School of Engineering and Applied Science, University of California, Los Angeles (UCLA), Los Angeles, CA, 90095, USA. *Corresponding email: yhu@seas.ucla.edu
† These authors contributed equally to this work.

temperature drop ΔT across an interface when a heat flux q'' is applied¹⁴:

$$\text{TBR} = \frac{\Delta T}{q''} \quad (1)$$

The total TBR consists of several parts (Figure 2): one is the intrinsic interface scattering of energy carriers (e.g., phonons and electrons) attempting to traverse the interface—the probability of transmission after scattering will depend on the available energy states on both sides of the interface; and the other part is near-interfacial volume resistance, due to incomplete contact or disorders near interface, such as interface roughness and voids, poor crystalline quality, defects, grain boundaries, and impurities. The latter part can be minimized through improved materials quality, but the first part has been found existing at all heterogeneous interfaces even with atomic perfection. Swartz and Pohl studied metal/dielectric interfaces at temperatures lower than 100 K, in which range the phonon transmission across interface was found similar with acoustic waves¹⁴. Since then, various factors which may affect TBR have been intensively explored, including interface disorder, roughness, bonding strength, vibrational spectrum mismatch, material anisotropy, external field and so on.

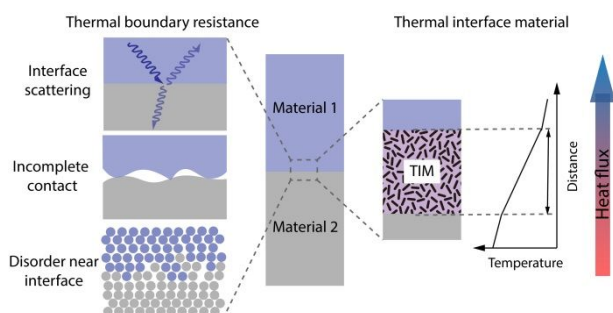


Fig. 2 Materials components of TIM and contributions to TBR. Schematic showing the multi-scale contributions to a lumped TBR, including the atomistic interface scattering to incomplete microscale contacts and disorders near the interface. The TBR results in a temperature drop across the interface and is expected to be improved using TIM.

2.1.1 Theoretical foundation to consider interface energy transport and TBR. Despite decades of efforts, understanding and improving interface thermal transport still remains challenging. One general approach to consider energy transport across an interface is based on the Landauer-Büttiker formulation. This formulation treats interface problem by considering the flux of energy carriers (i.e. electrons, phonons, and etc.) irradiating the interface, scattered, and transmitted through (Figure 3). The initial Landauer formula^{15, 16} was suggested to study transport phenomena in the quantum regime and relate the electrical resistance of a quantum conductor to the scattering properties. Later, a generalized Landauer-Büttiker formula^{17, 18} was developed to further expand the description in terms of transmission probabilities. With the progress in nanotechnology and condensed matter physics, experiments¹⁹⁻²¹ have shown good agreement with

the formula predictions, for example in the ballistic transport regime. Later, the theory was applied to analyze thermal energy transport across interface under equilibrium at temperature T ²²

$$q'' = \frac{1}{2(2\pi)^3} \sum_i \int_{\mathbf{k}} \tau_{AB} \cdot E \cdot \mathbf{v} \cdot \mathbf{n} (f_A - f_B) d\mathbf{k} \quad (2)$$

where E , \mathbf{k} , i , f , \mathbf{v} are the energy, momentum, band branch, distribution function and group velocity of heat carriers and \mathbf{n} is the unit vector normal to interface between material A and material B. The transmission coefficient τ_{AB} for heat carriers is the key parameter to determine TBR. Eq. (2) can be applied to both phonons and electrons, where the distribution function is respectively the Bose-Einstein or Fermi-Dirac distribution²³. One implication of this formulation is the absence of coupling effects between different carriers and inelastic scattering. For example, since the phonons are quasiparticles, two phonons can merge into single phonon, or one single phonon can split into two phonons -- The number of quasiparticles in this process is not conserved, which breaks the underlying assumption of Landauer-Buttiker formulation. However, Landauer-Buttiker formulation is still widely applied because of its success regarding the consistence with certain experimental results and the lack of better established methods to consider the interacting of carriers at interface.

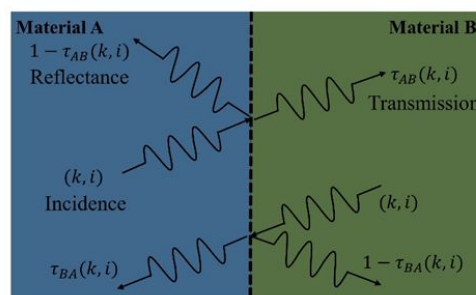


Fig. 3 Interface phonon transport between Materials A and B. Mode-specific phonons with different wavevector \mathbf{k} and polarization i have different transmission probability τ when they are across the interface

2.1.2 Phonon picture. In dielectric solids such as semiconductors, ceramics, oxides, and even polymers, heat is mainly carried by lattice vibrations, and therefore TBRs are usually quantified based on phonons, i.e. the quantum mechanical modes of lattice vibrations²⁴. The resistance to heat flux can be understood as resulted from the breakdown of coherence of energy carriers' transport across the interface. When the incident phonons encounter the interface, reflection and transmission happens simultaneously as illustrated in Figure 3. The Landauer-Buttiker formulation can be adapted to the phonon system^{14, 23}

$$\frac{1}{\text{TBR}} = \frac{1}{2(2\pi)^3} \sum_i \int_{\mathbf{k}} \tau_{AB}(\mathbf{k}, i) \hbar \omega(\mathbf{k}, i) |\mathbf{v}(\mathbf{k}, i) \mathbf{n}| \frac{df}{dT} d\mathbf{k} \quad (3)$$

Under phonon picture, all parameters here are as a function of phonon mode or frequency: $\tau_{AB}(\mathbf{k}, i)$, $\omega(\mathbf{k}, i)$, $\mathbf{v}(\mathbf{k}, i)$, f are the mode-dependent transmission coefficient, phonon frequency, group velocity and equilibrium Bose-Einstein distribution

function corresponding to phonons with wavevector \mathbf{k} and polarization i . From the Landauer-Buttiker formulation, it can be pointed out that TBR is significantly affected by the phonon density of state and group velocity, both of which can be obtained from phonon band structure. Temperature can also affect TBR. Other important factors that could affect the transmission coefficient or TBR include the interface bonding, roughness, and disorder. In the following, these major factors determining TBR are discussed.

Phonon band structure. The spectral phonon heat flux across interfaces requires a detailed knowledge of the phonon band structures of materials. Experimental techniques such as neutron scattering and X-ray scattering can be used to measure the phonon dispersions but are limited due to the high economic and time cost. For a long time, the Debye approximation had been used for the approximation to phonon band structure, in which the phonon frequency is linear with its wave vector. A simplified estimation from the Debye model is that a better match of phonon density of states, or Debye temperature can usually reduce the TBR. However, the Debye approximation oversimplifies the calculation using a single phonon group velocity along each direction, therefore gives an overestimated strong temperature dependence of TBR due to the incorrect treatment of high-frequency phonons, and cannot account for anisotropic materials properties. Reddy and Majumdar²⁵ improved the Debye approximation by using the Born-von

Karman model instead of the linear assumption in the Debye model. Dames and co-workers²⁶ proposed elliptical dispersion relations to account for the anisotropic phonon band structure. More recently, Li and Hu¹³ performed ab initio calculations using density function theory to obtain the full phonon dispersion relationship over the entire Brillouin zone and successfully constructed the phonon mode-dependent modeling of the interfacial thermal transport. With the ab initio calculated phonon band structures from density functional theory and molecular dynamics simulation, these atomistic modeling work in combination with the experimental measurement together clearly quantifies the fundamental structure-property relationship between TBR and the intrinsic phonon band structures¹³. For example, the phonon band structure of highly anisotropic black phosphorus can also be accurately calculated for illustrating the anisotropy effects on TBR in Figure 4a-d. The velocity distribution and phonon density of states can be extracted from phonon band structure as shown in Figure 4e-f. The distinct phonon group velocity along different directions partially determines the anisotropic thermal energy transport across interfaces. The calculation based on Landauer-Buttiker formulation, facilitated by ab initio calculated phonon band structures, show consistency with the experimental measurements in predicting the anisotropic TBRs (Figure 4g-h), with a record-high anisotropic ratio up to 327% between different crystal orientations of a metal-semiconductor interface¹³.

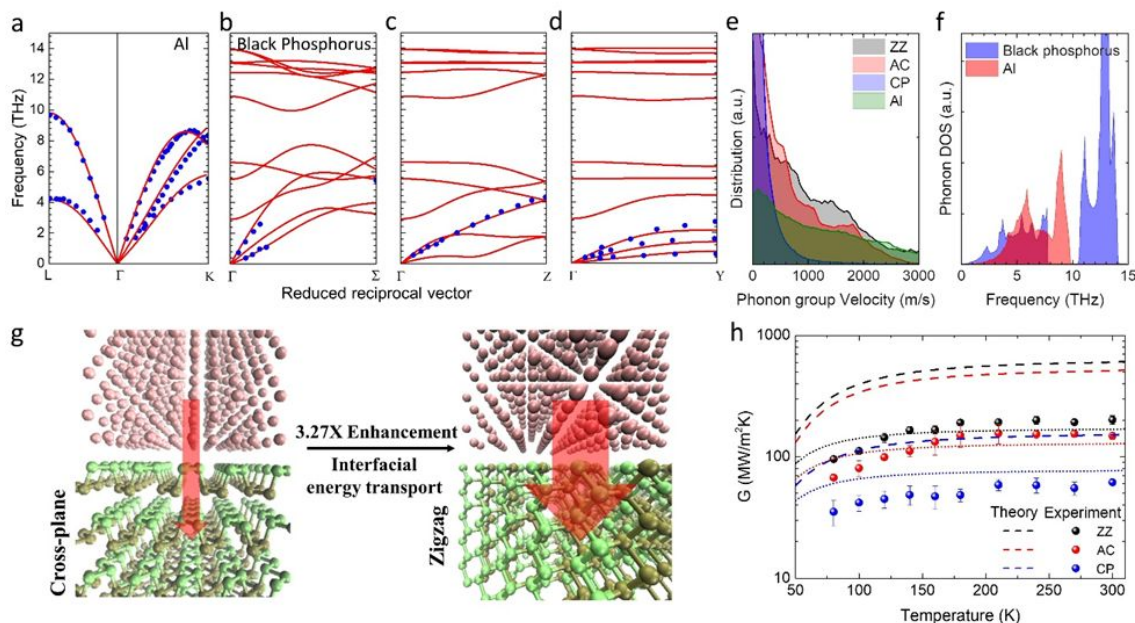


Fig. 4 Atomistic modelling of TBR. (a-d) Calculated materials properties on two sides of the interface (Al and black phosphorus)¹³, including (a) the Phonon band structures, (b) Phonon velocity distributions, and (f) the phonon density of states. (g) Illustration of the anisotropic TBRs between Al and black phosphorus along different crystal orientations, with experimental measurements and modeling results of temperature-dependent TBRs shown in (h)¹³. Reproduced with permission from ref. 13, copyright 2019 Wiley-VCH.

Temperature. Temperature can have a direct impact on TBR, for example, through the phonon distribution functions and heat capacity. In general, higher temperature can excite more phonons at high energy levels and enhance the total thermal energy across the interface. Experimentally, TBR is usually measured to increase along with temperature and saturates at high temperatures. The temperature dependence of TBRs is important to reveal the underlying transport mechanisms across different interfaces.

Interface conditions. In general, strong interface bonding can reduce TBR and improve heat dissipation. Intuitively, the interface bonding is expected to affect the transmission coefficients. Efforts in enhancing interface bonding include improving bonding from van der Waals to covalent types, tuning the surface wetting property from hydrophobic to hydrophilic using functional groups, or high pressure²⁷⁻³⁰. However it remains challenging to quantify the relationship. Other interface conditions such as roughness and disorder are also expected to modulate TBR.

2.1.3 Analytical calculations for interface transmission. It has remained challenging to consider interface transmission, especially under practical materials conditions. Under the phonon picture, the most popular approaches developed over decades to analyze TBR are the acoustic mismatch model (AMM) and diffuse mismatch model (DMM), which essentially treat the interface transmission in the following extreme cases and assume specular or diffusive interface scattering, respectively

Acoustic mismatch model. AMM was first introduced by Khalatnikov in 1952 to understand TBR between helium and solid³¹. For AMM, all the phonons are assumed to transmit through interface like the acoustic waves, i.e. acoustic phonon near the Brillion zone center. The transmission probability of acoustic waves has been well solved from the continuum elasticity equations³²

$$\tau_{AB} = \frac{4 \cdot Z_A Z_B}{(Z_A + Z_B)^2} \quad (4)$$

where Z is the acoustic impedance, product of density and sound velocity. Thus for AMM, the mass density and sound velocity of materials at the interface are the two deterministic factors for TBR. AMM usually works well at temperature lower than 30 K, where only low-frequency phonons near Brillion zone center are excited, meeting the assumption. At high temperature, AMM would significantly underestimate the TBR.

Diffuse mismatch model. In Swarts and Pohl's classic paper, DMM was proposed to predict TBR for diffusive interface. DMM assumes all the phonon are reflected diffusively and elastically to lose their memory after the scattering at the interface. This implies that every phonon has the same probability of transmission from one side and reflection from the other side. Mathematically, it can be described as

$$\tau_{AB}(k, i) = 1 - \tau_{BA}(k, i) \quad (5)$$

Considering the detailed balance of heat flux at interface¹⁴, the transmission coefficient can be derived as

$$\tau_{AB}(k, i) = \frac{\sum_i \int_k^{SideB} |v(k, j) n| \delta_{\omega_0, \omega(k, j)} dk}{\sum_i \int_k^{SideA} |v(k, i) n| \delta_{\omega_0, \omega(k, i)} dk + \sum_j \int_k^{SideB} |v(k, j) n| \delta_{\omega_0, \omega(k, j)} dk}$$

(6)

where $\delta_{\omega_0, \omega(k, i)}$ is the Kronecker delta function. In general, DMM predicts the lower limit for TBR. For materials with a large mismatch of phonon density of states, DMM usually overestimates the TBR because it doesn't account for the inelastic phonon scattering.

Radiation limit for interface transmission. Another model called radiation limit has been commonly used for evaluating the lower limit of TBR considering only elastic phonon transmission across an interface. In the radiation limit model, as long as they are allowed by the phonon band and density of states, all the phonons can transmit across the interface with a unitary transmission coefficient, i.e. $\tau_{AB}(k, i) = 1$. The radiation limit usually underestimates the TBR.

2.1.4 Contributions from electrons and other energy carriers to TBR. It should also be noted that energy carriers other than phonons could also contribute to heat transfer depending on materials. In addition to phonons, other particles (or quasiparticles), such as electrons, spinons, and magnons, can also carry thermal energy. When multiple heat carriers are present at interface, more heat conduction channels may be opened and the coupling between them would make the interfacial thermal transport more complicated. For example, a metal-dielectric interface may involve the coupling between phonons and electrons.

2.2 Modeling Frameworks

Over the last decades, atomistic models have been developed to gain more fundamental understanding of TBR, such as molecular dynamics (MD) simulation³³⁻³⁶, lattice dynamics^{37, 38} and atomistic Green's function (AGF)^{39, 40}. In the following, we briefly summarize the progress in interatomic potentials and ab-initio calculations as important modeling input, as well as different models with the discussions on their respective advantages and disadvantages in modeling TBR.

Empirical modeling and interatomic potentials. For most atomistic modeling techniques, the interatomic force between different atoms needs to be known for integrating the dynamical motion of atoms or constructing a set of Newtonian equations under the framework of lattice dynamics. Empirical interatomic potentials are commonly used for describing the interatomic force due to their simplicity and low cost of time. Some classic empirical potentials include the Lennard-Jones potential for van der Waals interaction, embedded atom model for metallic interactions, Stillinger-Weber potential and Tersoff potential for covalent bonding⁴¹⁻⁴⁴. All these empirical potentials are fitted from experimentally measured material properties or quantum mechanical calculations. Unfortunately, there is no universal potential that is capable to describe all the materials. An appropriate selection of empirical potentials is important for calculating thermodynamics properties. Nowadays, more advanced potentials are developed to give better accuracy in describing interatomic forces. For example,

reactive force field based on the principles of quantum mechanics can even predict the bond breaking and formation⁴⁵. However, there could be a tradeoff between accuracy and simulation cost.

Ab-initio calculations. With the rapid development of computational power and techniques, ab initio calculation, for example, based on density functional theory (DFT) has been applied for calculation to avoid empirical potentials or fitting parameters. In DFT calculation, the multi-particles problem of n electrons can be simplified as a set of one-electron equations, i.e. Kohn–Sham equations⁴⁶. Once the electron density is solved, the force between different atoms can be computed from Hellmann-Feynman theorem. The ab initio method can improve the accuracy of interatomic forces and be used to construct harmonic matrix despite of an increased computational cost. Such DFT-based approach has been applied for electronic calculations for decades but for phonons more recently^{47–50}.

Molecular Dynamics. In MD simulations⁵¹, the dynamical trajectories, velocities and forces of atoms are simulated following Newton's equation of motion. The macroscopic thermodynamic properties, like temperature and heat flux can be derived from the simulated microscopic properties. The interaction between atoms is described under empirical force field or derived from quantum mechanical calculations. As the higher order anharmonic force is included in MD simulations and the inelastic scattering of phonons is implicitly included. Moreover, because MD simulations attempt to simulate the temporal evolution of atomic system in real space, the phonon picture is not necessary. The interfacial thermal transport across materials where the definition of phonons is ambiguous, e.g. liquid and amorphous polymers, can also be studied. Note

that, MD is currently the only method that can treat interfaces system with practical conditions; other modeling methods such as Green's function formalism idealizes the settings such as perfect epitaxial interfaces. There are mainly two different approaches for studying interfacial thermal transport, i.e. nonequilibrium MD (NEMD)³³ and equilibrium MD (EMD)³⁵. In NEMD, the steady state thermal response near the interface to a certain temperature gradient can be monitored as illustrated in Figure 5a–b¹³. By recording the heat flux and temperature drop at the interface, the TBR can be directly calculated according to Eqn. (1). By combining the NEMD and DMM with experimental measurements, the effect of anisotropic structure on TBR is revealed recently. NEMD has been applied to calculate TBR along different crystal orientations and show its anisotropy in agreement with the experimental results and DMM calculation¹³. In EMD, the fluctuation of heat flux across interface is monitored when the system is under thermal equilibrium at a given temperature T . The TBR can be derived from the fluctuation-dissipation theorem and the Green-Kubo formula

$$\frac{1}{TBR} = \frac{1}{Ak_B T^2} \int_0^\infty \langle Q(t)Q(0) \rangle dt \quad (7)$$

where A , k_B , Q and $\langle \dots \rangle$ denotes respectively the interface area, Boltzmann constant, interfacial heat exchange at a certain time t and ensemble average. Figure 5c illustrates the autocorrelation function of heat exchange at the interface between Si and Ge, i.e. $\langle Q(t)Q(0) \rangle$, from EMD³⁵. The TBR can be calculated from Eqn. (3) as shown in Figure 5d. To analyze the modal contributions to TBR, the interfacial heat exchange can be projected to different phonon modes and the TBR calculated from Eqn. (3) can be decomposed into different phonon modes.

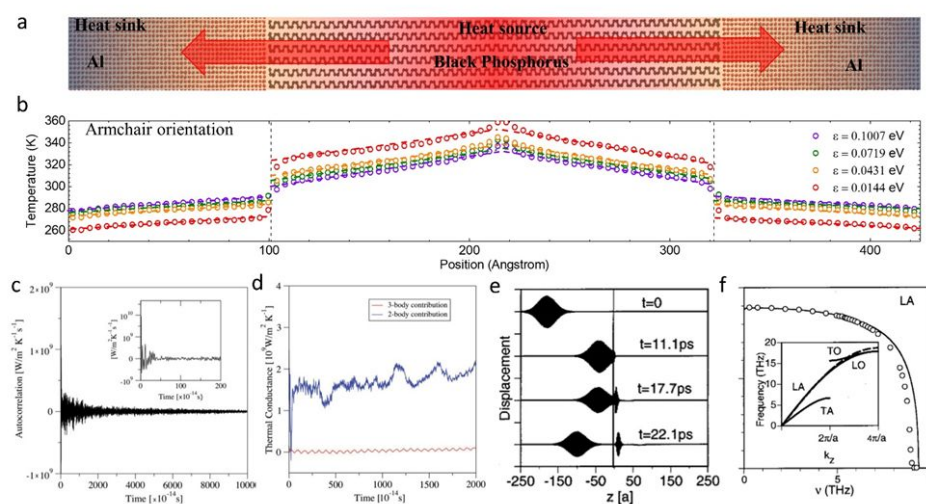


Fig. 5 Atomistic modelling methods for interfacial thermal transport. (a) Atomistic configuration in nonequilibrium molecular dynamics (MD) simulation of thermal transport across interface between Al and black phosphorus and (b) the calculated temperature profile across the junction¹³. Reproduced with permission from ref. 13, copyright 2019 Wiley-VCH. (c) Autocorrelation function of heat flux at interface between Si and Ge from equilibrium MD simulation and (d) the calculated TBR³⁵. Reproduced with permission from ref. 35, copyright 2012 American Physical Society. (e) Illustration of phonon transmission at imaginary interface from wave-packet simulation and (f) the calculated spectral transmission coefficient calculated from wave-packet simulation⁵². Reproduced with permission from ref. 52, copyright 2002 American Institute of Physics.

Nowadays, due to the availability of many open-source codes for MD simulation and the simplicity to implement MD simulation for TBR calculations, it has been applied to different TIM systems.

Wave packet. The wave-packet method⁵² is a numerical method studying the transmission of a single wave packet across interface within the framework of MD simulation. In this method, the wave packet is created by linear combinations of vibrational eigenstates. The atoms are carefully displaced to generate a wave packet with a certain wave vector and polarization. This method was first implemented by Schelling *et al.* to study the phonon scattering at imaginary interfaces (Figure 5e). The main advantage of this method is to study the transmission of single phonon mode and obtain the spectral transmission coefficient by varying the wavevector and polarization as illustrated in Figure 5f. One limitation of wave packet is that it cannot be used at high temperature because the thermal noise would overwhelm the wave packet signal.

Atomistic Green's function. AGF is another atomistic modelling method for TBR based on the Landauer formalism. In the field of thermal transport, it was early implemented for phonon transport in Si nanowire coated with amorphous layer and gained its popularity for the TBR calculation of numerous interfaces, e.g. Si/Ge, Cu/graphite and Mg₂Si/Mg₂Si_{1-x}Sn_x. Essentially, AGF method obtains the phonon transmission coefficient by solving a set of Newtonian equations under the framework of lattice dynamics. Due to the complexity brought by anharmonic force, most calculations for TBR based on AGF only consider harmonic forces. The transmission function $\tau_{AB}(\mathbf{k}, i)$ can be obtained from the Caroli formula⁵³,

$$\tau_{AB}(\mathbf{k}, i) = \text{Trace}(\Gamma_A G \Gamma_B G^\dagger) \quad (8)$$

where Γ_A and Γ_B are escape rates, and G is the Green's function, representing the response of the system to an infinitesimal perturbation. Since the harmonic matrix in AGF calculation can be constructed from force constants from the DFT calculation, the AGF method is believed to correctly capture the interfacial interaction especially at near perfect interfaces. The main advantage of AGF is to resolve phonon mode information at the interface. However, the first principle AGF calculations can be computationally formidable if the supercell of interface is too large due to large lattice mismatch of the materials interface; to include anharmonic effects for practical interface conditions may pose additional challenge⁴⁰.

2.3 TBR at practical materials interfaces

The above discussions are focused on the atomistic consideration of interface scattering and TBR. For practical materials interfaces, however, additional thermal resistance may come from other factors such as incomplete contacts and disorders near interface. As illustrated in Figure 2, the materials components of TIM and different contributions to a (lumped) TBR are discussed in the following.

Disorder near interface. TBR could also be caused by disorder interface of different materials. Due to the materials growth or fabrication processes, it may consist of an

interphase region of appreciable thickness with properties much different than those of the materials on either side. For example, for the chemical growth of GaN, GaN/AlN transition or adhesion layers are usually used for diamond or silicon carbide substrates because of the large lattice mismatch. The thermal stack from these transition layers produces additional TBR and prevents achieving the full benefit of using high-conductivity substrates.

Incomplete contact. TBR could be caused by incomplete physical contact between two sides of the interfaces. When two similar or different fillers are in contact and form a junction, only a small portion of the actual surface area is involved due to the non-planarity and roughness of the contact surface; this causes contact thermal resistance. At this time, heat transfer at the junction can only occur through the actual contact area. In a more extreme case, it can even result in some air-filled gap trapped within the rest of the area, which is depicted in Figure 2. If we neglect the heat transfer by radiation between the surfaces, the heat flux go through this interface by two different heat conduction paths: solid-to-solid conduction through the contact points and conduction through the air trapped within the rest of the area, which is a poor thermal conductor compared to the solid materials. The heat transfer between different materials is limited by two different heat conduction paths which defined as thermal interfacial resistance. Therefore, in order to improve the heat transfer performance between heterogeneous interfaces and minimize the temperature drop across the junction, controlling TBR using TIMs is one primary solution.

3. Experimental methods to characterize TIMs

In this section, we summarize the typical experimental techniques for characterizing thermal properties of TIMs by starting with the underlying equations governing temperature and heat transfer,

$$Q = \kappa A \frac{\Delta T}{L} \quad (9)$$

$$\frac{\partial T}{\partial t} = \frac{\kappa}{\rho c_p} \left(\frac{\partial^2 T}{\partial x^2} + \frac{\partial^2 T}{\partial y^2} + \frac{\partial^2 T}{\partial z^2} \right) \quad (10)$$

Equation (9) and (10) are respectively the Fourier law and heat diffusive equation, where κ , A , $\frac{\Delta T}{L}$, ρ , c_p are thermal conductivity, cross-sectional area of heat flux, temperature gradient along the heat conduction direction, density and specific heat respectively. Experimental techniques can be categorized into steady-state methods when the measurement is performed after the thermodynamic properties of the system become time independent, or transient methods when the measured signals are temporal evolution of temperature. Most steady-state methods directly measure thermal conductivity according to Fourier's law. The key parameters to be measured are heat flux and temperature gradient. For example, the reference bar method and microbridge method is heat conduction experiment along a one-dimensional direction of interest. When two- or three-dimensional heat conduction experiments are performed, the thermal conductivity can be fitted by compare the steady state temperature profile with

the solution of time-independent heat conduction equation. For example, the Raman thermometry and infrared camera are commonly used in these indirect steady-state experiments. For transient measurement methods, the experiment is analyzed based on the measured temperature with solution of the differential heat conduction equation. The key signals for transient method are the temporal and/or spatial temperature evolution. For example, common transient measurement methods include hot-wire method, laser flash method, 3 ω method, photoacoustic method, Angstrom methods and thermoreflectance methods. In the following, we discuss in more details of different experimental methods.

3.1 Steady-state measurement

3.1.1 Reference bar method

Thermal conductivity is determined by measuring the temperature difference ΔT at a given distance under the steady state heat flow Q . The testing sample is placed serially with the reference materials with known thermal conductivity between a heat source and a heat sink. A steady state power input is applied and the resulting temperature profile across the sample and reference materials is measured by temperature sensors after a steady state temperature distribution is established⁵⁴. The temperature sensors can be thermocouples, thermistors or infrared thermometer. As the heat flow remains the same for the reference materials and the sample, it can be calibrated from the temperature gradient in the reference materials. Thereafter, the thermal conductivity κ of the TIM sample can be determined using Fourier's law of heat conduction with the measured temperature gradient and calibrated heat flow. Note that the reference bar method usually requires the testing sample to be relatively large and in standard shape, thus may not be suitable for micro/nanoscale samples. To ensure a steady state temperature distribution, sometime the test can take a long waiting time. In addition, the heat dissipation from other pathways such as convection needs to be negligible.

3.1.2 Microbridge method

Microbridge method was originally developed to reveal the high thermal conductivity of individual carbon nanotube^{55, 56} and further expanded to measure other nanostructures⁵⁷⁻⁶⁰. In this method, the sample is suspended between two micrometer pads, like a microbridge. Platinum wires are coated on these two pads to provide uniform joule heating to the pad and also serve as a resistance thermometer. The heat flux through the sample is usually applied by a joule heating power. Meanwhile, the temperature drop across the sample is measured using a micro fabricated thermometer. The thermal conductivity can then be determined from the Fourier's law. This method can be applied to nanostructures, especially in the form of 1D or 2D, such as carbon nanotube, graphene, black phosphorus. However, this method usually requires complicated microfabrication process and the careful calibration of the contact resistance between sample and the pads.

3.1.3 Raman thermometry

Raman peaks are related with the phonon properties of materials as they usually result from the interaction between optical phonons and incident photons⁶¹. The peak position, intensity or full width at half maximum can be calibrated with temperature-dependence. The temperature response of the sample to incident laser, for example under different power can be obtained and used to extract the thermal properties. Raman spectra has been applied in literature to measure varied bulk materials and nanostructures. However, the reliable thermal measurement using Raman thermometry requires careful calibration of laser absorption and temperature measurement. In addition, the coupling between thermal effect and other contributions such as thermal expansion can complicate the data analysis and measurement reliability.

3.2 Transient methods

3.2.1 Hot-wire method

Hot wire method is based on the transient heat conduction model of an infinitely long cylinder with a line heat source at the center⁶². Due to the convenience to implementation, it has been applied on a wide range of materials, including polymer composites. In this method, a metal wire is embedded in the sample, serving as a line heat source. After a constant current is supplied, the uniform Joule heating of platinum wire will start to heat up the whole sample. Once the sample radius is much larger than the heat diffusion length during sampling time and the diameter of platinum wire is thin and long enough, the differential heat conduction can be solved to give the temperature evolution described by the following equation

$$T(r,t) = \frac{P}{4\pi\kappa L} \left[\ln \left(\frac{4\alpha t}{r^2} \right) - \gamma \right] \quad (11)$$

where P is the Joule heating power, κ thermal conductivity, L length of the hot wire, α thermal diffusivity, t time, r the distance between wire center and interested point, and γ higher order terms regarding t and r , which can be neglected in most experiments. Thus, the thermal conductivity of the sample can be calculated if the slope of temperature rise versus the logarithmic value of time is known:

$$\kappa = \frac{P}{4\pi L \cdot \text{slope}} \quad (12)$$

To measure the temperature rise in the sample, a thermocouple or thermoresistor can be embedded inside the sample. The resistance change of platinum wire can also be used for sampling temperature change, so a more convenient way is to use a platinum wire as both heating source and temperature sensor as illustrated in Figure 6a⁶³. For hot-wire measurement, it is important to ensure a good thermal contact between metal wire and the sample material.

3.2.2 Laser flash method

The laser flash measurement is a non-contact method to measure the thermal diffusivity of materials. A typical measurement schematic of laser flash method is depicted in Figure 6b⁶⁴. An pulsed light source is used to uniformly heat up the sample's front side, and a temperature detector measures the time dependent temperature response rise at the rear side.

Heat conduction inside the material is taken as one-dimensional (i.e., no lateral heat loss). Time-dependent rear-side temperature response curve is fit to obtain the thermal diffusivity. Theoretically, the temperature rise at the rear side as a function of time can be written as:

$$T(t) = \frac{q}{\rho c_p d} \left[1 + 2 \sum_{n=1}^{\infty} (-1)^n \exp\left(-\frac{n^2 \pi^2}{d^2} \alpha t\right) \right] \quad (13)$$

where d is the TIM thickness, and α is the TIM's thermal diffusivity. By recording the temperature rise at the rear side, the thermal diffusivity α can be calculated by:

$$\alpha = \frac{1.38d^2}{\pi^2 t_1} \quad (14)$$

where t_1 is the characteristic time that takes for the sample to heat to one-half maximum temperature on the rear surface and usually used for analysis. The mass density ρ and specific heat c_p are needed for extracting the thermal conductivity $\kappa = \alpha \rho c_p$. During laser flash measurement, a good thermal insulation between the sample and the environment is important; otherwise, the characteristic time of the temperature peak would be incorrectly estimated.

3.2.3 3 ω Method

In 3 ω method, an AC at frequency ω passes through the heater/sensor $I(t) = I_0 \cos(\omega t)$, where I_0 is the current amplitude, which results in joule heating of the resistive heater at 2 ω frequency⁶⁵. Such a 2 ω heating leads to temperature change of the heater/sensor also at 2 ω frequency: $\Delta T(t) = \Delta T_0 \cos(2\omega t + \varphi)$, where ΔT_0 is the temperature change amplitude, and φ is the phase. The temperature change produces the heater/sensor's electrical resistance at 2 ω : $R_e(t) = R_{e,0} [1 + \alpha_R \Delta T_0 \cos(2\omega t + \varphi)]$, where α_R is the temperature coefficient of resistance of the heater/sensor, and $R_{e,0}$ is the heater/sensor's electrical resistance at the initial state. When multiplied by the 1 ω driving current, a small voltage signal across the heater/sensor at 3 ω frequency can be detected:

$$V(t) = R_{e,0} I_0 \cos(\omega t) + \frac{1}{2} R_{e,0} I_0 \alpha_R \Delta T_0 \cos(\omega t + \varphi) + \frac{1}{2} R_{e,0} I_0 \alpha_R \Delta T_0 \cos(3\omega t + \varphi) \quad (15)$$

This change in voltage at 3 ω frequency is measured to analyze thermal properties of the sample. Figure 6c shows a typical schematic of the 3 ω measurement. A metallic strip (e.g., aluminum, gold, and platinum) is deposited as both an electrical heater and a temperature sensor. Depending on the width of the heater, both the cross-plane and the in-plane thermal conductivity of the sample can be measured using the 3 ω method. For isotropic materials with thickness larger than the heat diffusion length, the temperature rise can be approximated as

$$\Delta T_0 = \frac{p}{\pi L \kappa} \left[0.5 \ln\left(\frac{\alpha}{a^2}\right) - 0.5 \ln(\omega) + \eta \right] - i \left(\frac{p}{4L\kappa} \right) \quad (16)$$

where p/L is the peak electrical power per unit length, $2a$ the width of the metallic strip, η a constant. Thermal conductivity is obtained by fitting the experimentally measured temperature rise data under a variety of heating frequency ω to Eq. (13).

A significant advantage of the 3 ω method compared to the steady-state methods is that the error due to radiation heat loss is greatly reduced. For electrically conducting and semiconducting materials, samples need to be electrically isolated from the metallic heater/sensor with additional insulating layer, the extra thermal resistance introduced by which needs to be considered in terms of sensitivity and measurement accuracy.

3.2.4 Photoacoustic technique

A test fixture for a photoacoustic measurement is shown in Figure 6d. In the photoacoustic technique, a laser heats a sample that is in a photoacoustic cell⁶⁶. This results in the sample heating and through conduction with the surrounding gas, a change in pressure of the gas occurs which is sensed in the form of an acoustic wave. An attached microphone senses this wave and its phase and amplitude are recorded, which is used to determine the thermal properties of the sample. One advantage of this method is its applicability to thin layer samples, for example carbon nanotube array TIMs⁶⁷.

3.2.5 Angstrom and infrared microscopy enhanced method

The thermal measurement based on the steady-state temperature oscillation to periodic heating was first invented by Angstrom in 1861⁶⁸ and has been widely applied on thin films afterwards. As shown in Figure 6e⁶⁹, the film sample is usually suspended and heated using a sinusoidal heat source. The temperature response of the thin film sample at two different locations are monitored. By comparing the temperature oscillation amplitude T_1 and T_2 and phase difference $\Delta\varphi$, the thermal diffusivity can be calculated from the following equation

$$\alpha = \frac{\omega \Delta x^2}{2\Delta\varphi \ln(T_1/T_2)} \quad (17)$$

where ω , Δx , are the angular frequency of heating power and distance between two detection points. By utilize the infrared microscopy, the Angstrom method can be extended to films with lateral size of millimeters and thickness of micrometers as long as the sample can be suspended. The Angstrom method is usually limited to thin film samples, in addition to the challenge in suspending the sample and minimizing heat loss by thermal radiation from sample surface.

3.2.6 Ultrafast optical pump-probe measurement

Thermal measurement techniques based on ultrafast optics include time-domain thermoreflectance (TDTR)⁷⁰⁻⁷², frequency-domain thermoreflectance (FDTR)⁷³ and transient thermal grating (TTG) methods⁷⁴. In each of these techniques, a pump laser beam deposits heat into the sample, which consists of the substrate of interest coated with a thin metal transducer film. The change in temperature due to this heat input is monitored with a probe beam. The thermal properties can be extracted by fitting the measured data with the prediction of a thermal model.

The time-domain thermoreflectance (TDTR) technique is a non-contact optical method to measure thermal properties (thermal conductivity, interfacial thermal conductance, and heat capacity)⁷⁰⁻⁷². As illustrated in Figure 6f, in TDTR method, a femtosecond ultrafast pulse laser beam is splitted into two laser beams, called pump and probe beams. A metal thin film

is usually coated on sample surface to serve as a transducer that absorbs the pump laser energy to heat up the sample and generate an instantaneous temperature rise. The surface temperature can be detected from the reflectance of the metal transducer as its reflectivity is linearly proportional to temperature changes. During the TDTR measurement, the transient temperature decay is continuously recorded versus the delay time between pump and probe with a sub-picosecond temporal resolution. The temperature decay is fitted with thermal model to obtain the thermal properties of the sample. FDTR is a frequency-domain technique where the pump laser beam is a sinusoidally modulated CW laser beam⁷². This sinusoidal heat input creates a temperature wave with the same amplitude and phase relative to that of the heat input. We measure the amplitude and phase of this temperature wave as a function of modulation frequency with a second probe beam and a lock-in amplifier. The thermal conductivity is obtained by comparing the observed response with the predictions of a thermal model. TTG technique using two crossing pump pulses to create a sinusoidal interference pattern, which induces a sinusoidal temperature response on the sample surface after absorption⁷⁴. The temperature profile and the resulted acoustic wave modulate the complex index of refraction of the material to create a sinusoidal time dependent grating that diffracts the probe beam. The diffracted signal is detected and analyzed for thermal properties. TTG can be used for thermal conductivity measurement but usually requires the sample to be of thin film and specific optical properties and is not suitable for TBR measurement. Compared with micro-fabricated devices and 3ω methods, these optical methods can be used to perform non-contact and fast thermal conductivity measurement on both bulk and nanoscale samples.

TDTR technique, in particular due to its high sensitivity and flexible adaptability, has been widely applied to explore thermal properties of different materials ranging from low thermal conductivity silica aerogels^{7, 75} (~ 0.01 W/mK), van der Waals crystals^{76, 77} (~ 0.5 W/mK), to high thermal conductivity boron phosphide⁶ (~ 500 W/mK) and boron arsenide⁵ (~ 1300 W/mK), and to thermal boundary resistance¹³. Anisotropic thermal properties are of both fundamental and practical interests, but remain challenging to characterize using conventional techniques. Note that conventional TDTR assumes isotropic heat conduction; most other techniques requires the alignment of sample orientation of interest along with the temperature gradient when dealing with anisotropic samples. Recently, a new technique based on asymmetric beam time-domain thermoreflectance, i.e., AB-TDTR⁷⁸, is developed to accurately measure three-dimensional anisotropic thermal transport by extending the conventional TDTR technique. Using an elliptical laser beam with controlled elliptical ratio and spot size, the experimental signals can be exploited to be dominantly sensitive to measure thermal transport along the cross-plane or any specific in-plane directions⁷⁸.

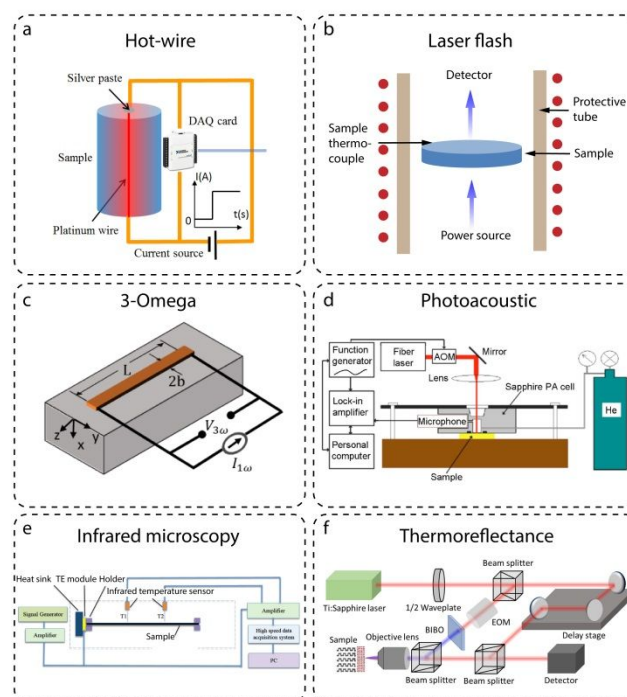


Fig. 6 Experimental techniques for thermal measurement. (a) Hot-wire method⁷⁹. Reproduced with permission from ref. 79, copyright 2019 Wiley-VCH. (b) Laser flash method. (c) 3-Omega method⁸⁰. Reproduced with permission from ref. 80, copyright 2015 AIP Publishing LLC. (d) Photoacoustic method⁶⁷. Reproduced with permission from ref. 67, copyright 2007 American Institute of Physics. (e) Infrared microscopy enhanced Angstrom method⁶⁹. Reproduced with permission from ref. 69, copyright 2016 Elsevier Ltd. (f) Time-domain thermoreflectance method¹³. Reproduced with permission from ref. 13, copyright 2019 Wiley-VCH.

4. Materials design for TIMs

The design of TIMs is a multi-disciplinary problem, requiring physical consideration of the thermal properties, contact mechanics, and even electrical and optical properties depending on applications. For the mechanical properties, the TIMs are typically made of materials that show good mechanical compliance, wetting capability, or can fill out the voids between the two surfaces, thereby increasing the effective contact area. The deformability requirement leads to their most fundamental engineering requirement: low mechanical shear strength to allow shape change and conformal interfacial contact. For the electrical properties, some electronics applications require TIMs to be of low dielectric constant, high electrical resistivity, high breakdown strength. The breakdown electric field of insulating materials is an important factor. The incorporation of inorganic fillers can significantly modify the breakdown electric field of a composite depending on the loading, shape, size, surface chemistry, dispersion, and electrical characteristics of the fillers. The electric field distortion and enhancement are caused by the difference in dielectric constant (for alternating current) or electrical conductivity (for direct current) between

the fillers and polymer matrix. As the difference becomes greater, the field distortion is intensified and the field enhancement is greater. Therefore, in order to obtain high breakdown-strength composites, one must choose fillers having similar electrical characteristics as the polymer matrix. For the thermal properties, there are several key parameters to be considered for the design of a TIM: contact resistances at the interface, thermal conductivity, and its thickness, which together determines a lumped TBR. First, the thermal contact resistance between the TIM and substrate is an important factor and can be affected by the conformity, how well the TIM fills out voids, and the atomistic scattering from mismatch as discussed in Section 2.1. It can also be affected by the compliancy of the TIM, how well it attaches to the substrates, and the applied pressure at the interfaces. To improve the overall thermal performance, this thermal contact resistance needs to be minimized. Second, the thickness of the TIM needs a balance. It is desirable to minimize the bond line thickness to reduce the whole thermal interfacial resistance; in addition, lower thickness means less material consumed and a lower cost. However, in practice, a too thin bond line can result in voids due to uneven TIM coverage as well as reliability issues during thermal cycling due to mismatch in coefficient of thermal expansion. In addition, for certain applications such as a thermal pad, the thickness can be limited by the handling and mechanical requirements. Therefore, the thickness design needs a balance over requirements from all these aspects. Third, the thermal conductivity of the TIM layer plays an important role in contributing a stray thermal resistance in series to the contact resistance. The thermal conductivity of the TIM determines how well the material conducts heat within the TIM itself, and thus is desired to be high. Commonly used TIMs are a variety of polymer-based matrix filled with high thermal conductivity particle inclusions, typically with diameter 2-25 μm . The effective thermal conductivity of TIM itself is typically on the order of 2 W/mK (i.e. a TBR of 5×10^{-5} m²K/GW for a 100 μm thick TIM layer). The resistance of commercial TIM products however is even lower to interfaces between the TIM and the device layer, as well as additional structural disorders and voids during integration. Another research area is using solders, which can provide better TBR and thermal conductivity using metallic alloys, however, are less attractive due to their mechanical stiffness and electrical conduction.

In the following part of this section, we discuss the materials design for TIMs with a focus on filler-matrix structures as most popularly investigated in literature study. We first discuss about the filler material from typical state-of-the-art filler materials to emerging new high thermal conductivity materials that could potentially make significant improvement by replacing the current filler materials. Next, for matrix materials, we discuss about typical matrixes based on polymers and metal solder matrix, as well as recent studies on developing high thermal conductivity polymers that could potential contribute to the matrix design. Furthermore, we provide a summary on the recent progress on structural design over TIM layers and discuss about the understanding and design

strategy on how to improve the further thermal performance of TIMs.

4.1 Filler materials

Filler-matrix structure is most widely used as TIMs due to its electrical insulation, easy processing, and low cost. Yet the commercial TIMs are still limited by the low thermal conductivity of matrix materials which is usually in the form of polymers due to the requirement in mechanics and filling efficiency. To improve its performance, high thermal conductivity fillers such as ceramics, metals, nanotubes and graphene are included usually in the form of nanoparticles into the matrix. Additionally, various methods in improving heat conduction have been investigated, ranging from surface functionalization, filler alignment, and structural optimization. More details about the recent progress are discussed in the following.

4.1.1 Typical filler materials

Several ceramic materials with a high thermal conductivity within 1-300 W/mK (Figure 7), such as aluminum nitride (AlN), boron nitride (BN), silicon nitride (Si₃N₄), silicon carbide (SiC) have been extensively explored as fillers due to their electrical insulation and stability. Aluminum oxide has a relatively lower thermal conductivity (~ 30 W/mK), but is among the currently most common used for commercial thermally conductive fillers due to its low cost and high electrical resistivity (Figure 8a)⁸¹. Boron nitride (BN) is another TIM filler intensively studied in recent literature due to its high thermal conductivity (200-600 W/mK) and dielectric property (Figure 8b)⁸². Graphene/graphite (Figure 8c), carbon nanotubes (CNTs) (Figure 8d) and nanofibers are also explored for TIMs fillers due to the high thermal conductivity. Monolayer graphene was reported to have high thermal conductivity over 1000 W/m \cdot K at room temperature. However, when assembled into bundles, thermal conductivity will degrade to be orders' lower due to the intrinsic ambient scattering. The intrinsic anisotropic thermal conductivity, i.e. high conductivity along the in-plane direction but very low conductivity in the cross-plane direction (e.g., 5 W/m \cdot K for graphite due to weak van der Waals bonding) pose another challenge in their applications. In addition, the thermal interfaces between fillers and matrix could involve additional scattering and significantly compromise the benefit from the high conductivity of fillers. For example, graphene-polymer and CNT-polymer composites often have thermal conductivities lower than 1W/m \cdot K even with high filler concentrations. This can be attributed to weak van der Waals bonding at the filler junctions where the phonon transport along the strong covalent bonding is largely impeded. In order to improve the heat transfer properties, covalently-bonded junctions in filler networks are reported in recent progress⁸³⁻⁸⁸.

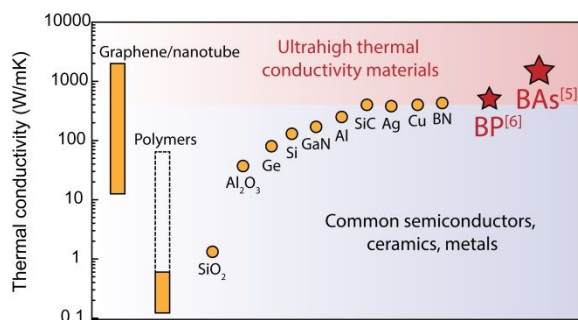


Fig. 7 Thermal conductivity of materials. Common semiconductors, ceramics and metals have the thermal conductivity within the range of 1-300 W/mK, including SiO₂, Al₂O₃, Ge, Si, GaN, Al. The industrial high thermal conductivity standards are copper and SiC, and materials with conductivity higher than 400 W/mK are considered as ultrahigh thermal conductivity materials, such as newly developed BAs (1300 W/mK)^{5, 89} and BP (~500 W/mK)⁶.

Metals in general have higher thermal conductivity (10 ~ 300 W/mK, Figure 7) than polymers so they have been used as the filler when electrical insulation and lightweight are not considered for the applications. Typical metal fillers include aluminum (Al)⁹⁰, silver (Ag) (Figure 8e)⁹¹, copper (Cu)⁸⁷, and nickel (Ni)⁹². Polymers modified with the inclusion of metallic particles include polyethylene, polypropylene, polyamide, polyvinylchloride, and epoxy resins, showing thermal conductivity performance depending on the thermal conductivity of the metallic fillers, the particle shape and size, volume loading, and alignment in the polymer matrix. Hybrid fillers using mixtures of different materials or different structural and geometric parameters are studied to improve the TIM performance⁹³. New kinds of fillers having hybrid compositions with large formation of conduction path networks is helpful to form percolating networks and improve maximum packing fraction, which increase the effective thermal conductivity. Different types of fillers with different shapes and sizes were used either alone or in combination to prepare new kind of thermally conductive polymer composites, including studies of BN/CNTs⁹⁴, BN/nanofibers⁹⁵ and graphene oxide/CNT⁹⁶ (Figure 8f) hybrid composites.

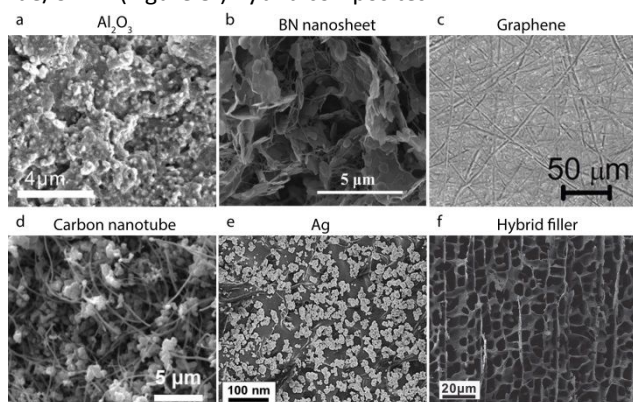


Fig. 8 Filler materials for TIMs. SEM images of most common fillers in polymer-based composite TIMs: (a) aluminum oxide⁸¹,

Reproduced with permission from ref. 81, copyright 2015 Elsevier Ltd. (b) boron nitride nanosheet⁸², Reproduced with permission from ref. 82, copyright 2017 Wiley-VCH. (c) graphene⁹⁷, Reproduced with permission from ref. 97, copyright 2012 American Chemical Society. (d) carbon nanotubes⁸⁶, Reproduced with permission from ref. 86, copyright 2016 Elsevier Ltd. (e) silver⁹¹ Reproduced with permission from ref. 91, copyright 2014 Royal Society of Chemistry. (f) hybrid fillers⁹⁸. Reproduced with permission from ref. 98, copyright 2018 Wiley-VCH.

4.1.2 Size effect of thermal conductivity and mean free path spectra

Size of fillers is also important for the overall performance of TIMs. The size of fillers in commercial TIMs spans usually from 2 to 25 μm. If the size of fillers is too large, the mechanical properties of TIMs may be compromised. On the other hand, the thermal conductivity of fillers can be lower than the bulk values when the filler size is too small. Such a reduced thermal conductivity can be attributed to the size effects introduced by boundary scattering.

In dielectric materials, thermal transport is dominated by a spectrum of phonons, which travel inside materials with different frequencies, wave vectors, group velocities. The average distance travelled by a phonon between two successive collisions are called phonon mean free path (MFP). Recent literature uses cumulative phonon MFP spectra to describe the accumulative contribution from phonon modes with specific MFPs^{99, 100}. For example, the cumulative phonon MFP spectra of diamond, graphene, BN, silicon, GaN, Al₂O₃ are plotted in in Figure 9a⁷: These phonons dominating heat conduction have MFPs ranging from 10 to 1000 nm in Al₂O₃, from 100 nm to 10 μm in GaN, BN, graphene and diamond, from 100 nm to 100 μm for Si. When particle size is smaller than the MFP, additional boundary scattering will further reduce thermal conductivity. The MFP spectra can largely vary for different materials. Developing new techniques to achieve spectral mapping of thermal conductivity has been a significant advance in recent literature. The general measurement mechanism is illustrated in Figure 9b: Thermal transport in the materials with size-dependent heating down to the nanoscale are systematically measured. When the heating size is much larger than phonon MFP, heat is transferred diffusively following classical Fourier's law. When the heater size is comparable with or smaller than the phonon MFP, corresponding phonons with long MFPs would travel without scattering, experiencing ballistic transport. By utilizing the ballistic thermal transport caused by nanostructured heater, Hu *et al.* developed a spectral mapping technique to experimentally determine the phonon MFP distributions of different materials⁷. Moreover, the detailed diffusive to ballistic phonon transport information can be analyzed with multiscale modeling. For example, the size-dependent spectral heat flux in boron phosphide are carefully analyzed by Monte Carlo simulation and reconstruct the intrinsic phonon MFP spectra as shown in Figure 9c⁶. The fundamental understanding and experimental characterization of spectral

phonon transport in filler materials would provide important guidance for optimizing the thermal and mechanical properties of TIMs.

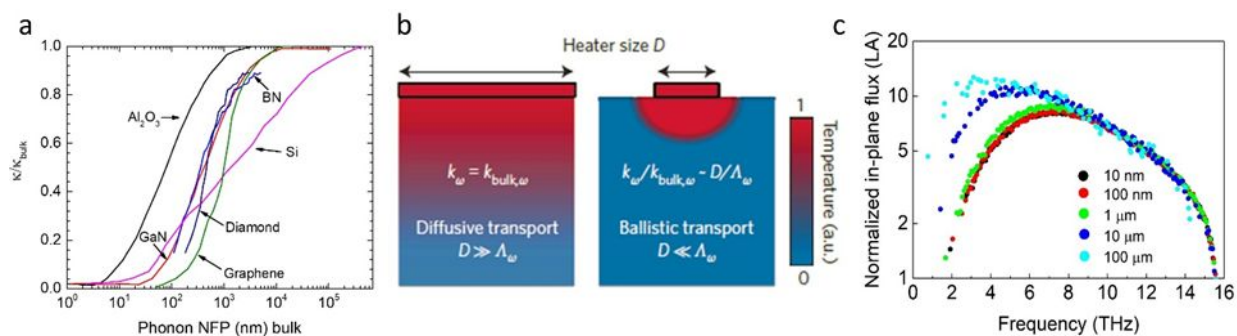


Fig. 9 Size effect of thermal conductivity and phonon mean free path spectra. (a) Phonon mean free path distributions for sapphire, GaN, Si, BN, diamond and graphene^{7, 101}. Reproduced with permission from ref. 101, copyright 2014 American Physical Society. (b) Thermal transport from diffusive regime to ballistic regime caused by heater size¹⁰¹. Reproduced with permission from ref. 7, copyright 2015 Springer Nature Limited. (c) Suppression of spectral heat flux by limited heater size⁶. Reproduced with permission from ref. 6, copyright 2017 American Chemical Society.

4.1.3 Emerging new high thermal conductivity materials

As summarized in Figure 7, typical semiconductors, ceramics, metals have the thermal conductivity within the range of 10–300 W/mK, including SiO₂, Al₂O₃, Ge, Si, GaN, Al^{102, 103}. The industrial standard materials for high thermal conductivity are copper and SiC, both with a thermal conductivity around 400 W/mK. Materials with thermal conductivity higher than 400 W/mK are rare and considered as ultrahigh thermal conductivity materials, such as diamond, cubic boron nitride, and carbon nanomaterials (CNTs and graphene)^{5, 104, 105}. Diamond is the most developed material for passive cooling of high-power electronics. However, the high cost, slow synthesis rates, low quality of diamond limit its development in industrial application. For carbon nanomaterials, including graphene and carbon nanotube, owing to its ambient interactions and disorder scattering as well as its anisotropic property, their thermal conductivity would reduce when assembled into practical sizes.

Discovering new high thermal conductivity materials is an emerging research frontier of critical importance for thermal management technologies including TIMs. The conventional criteria include simple crystal structure, light atoms, and strong bonding, which is prototyped by diamond but does not provide much insight in search for new candidates. Recently, ab initio calculation has investigated phonon spectra of binary compounds^{106–108}. In particular, a new semiconductor material, cubic boron arsenide (BAs) has been experimentally synthesized^{5, 109, 110} and measured with a record-high room-temperature thermal conductivity of 1300 W/mK⁵, beyond all common metals and semiconductors, as shown in Figure 10a–c. Experimental work has also verified that the distinctive band structure of BAs provides very long phonon mean free paths⁵. More recently, the basic mechanical, optical, and thermal properties of this new semiconductor were systematically characterized for the first time⁸⁹, which further verifies its promising applications for thermal management. Boron

phosphide (BP) is another emerging semiconductor with an ultrahigh thermal conductivity of ~ 500 W/mK (Figure 10d–f)⁶. In addition, BP processes highly refractory property and exceptional chemical inertness, hardness, and high thermal stability, which holds high promises for many practical applications. The successful development of ultrahigh thermal conductivity materials enables new application opportunities for thermal management and the design of thermal interface materials.

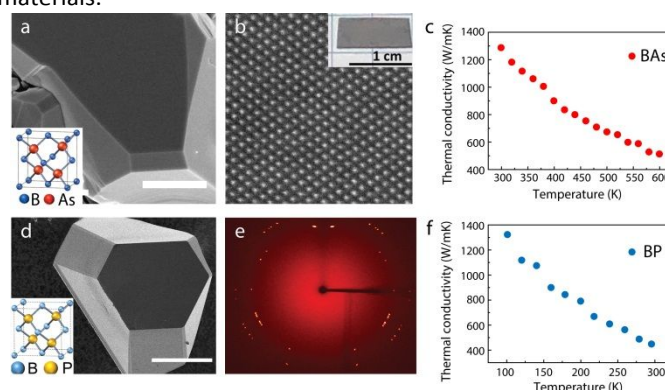


Fig. 10 Emerging ultrahigh thermal conductivity semiconductor materials, BAs^{5, 89} and BP⁶. (a) Scanning electron microscope (SEM) image of BAs. Scale bar: 5 μ m. Inset: schematic of the zinc-blende crystal structure of cubic BAs, resembling that of diamond. (b) TEM image of BAs showing atomically resolved lattices. (c) Temperature-dependent (300 to 600 K) thermal conductivity of BAs. Reproduced with permission from ref. 5, copyright 2018 American Association for the Advancement of Science. (d) SEM image of a sample of BP crystals. (e) Single crystal X-ray diffraction image of chemically synthesized BP crystals. (f) Measurement data of the temperature-dependent thermal conductivity from 77 to 298 K of BP. Reproduced with permission from ref. 6, copyright 2017 American Chemical Society.

4.2 Matrix materials

4.2.1 Typical polymer matrix

In electronic packages, the TIM is exposed to operating conditions which can adversely affect their properties and potentially lead to performance degradation like mechanical pump-out, delamination, cracking, and void formation¹¹¹. In order to minimize these issues, thermal-mechanical properties such as the elastic modulus, compressive property and interfacial adhesion property, and thermal expansion need to be characterized for the matrix. When a package undergoes temperature change, the mismatch in thermal expansion from different interfaces induces stresses. The package may undergo a shape change (convex to concave, or vice versa) which impacts the thermomechanical stress distribution. Therefore, a small elastic modulus is usually desired as a soft and flexible matrix enable better filling with the voids between the TIM and substrates. When subjected to multiple loadings, the application of TIMs may requires the capability to spring-back or recover its original shape upon deformation. In addition, it is essential to ensure good adhesion of TIMs to various surfaces like silicon die, integrated heat spreader lid, and heat sink for reliable thermal performance of the package.

Polymer-based TIMs are most widely used candidates as they are generally soft and flexible to overcome these mechanical issues^{10, 112, 113}. The idea for development of polymer-based heat exchanger benefit from the high molecular density, resistance to corrosion and fouling, easiness in processing and handling, vast mechanical properties, and comparable cost with other materials. Possibly, polymer can also offer high volume to weight ratio and be cost effective in comparison with other classic metallic heat exchanger materials. However, the intrinsic low thermal conductivity of polymers ($\sim 0.1\text{--}0.3\text{ W/mK}$) is the major drawback in thermal performance. Thus many efforts are using the suitable fillers within polymer matrix to improve the over performance of TIMs. Commonly used polymer matrix include polyethylene¹¹⁴, polypropylene¹¹⁵, polyamide¹¹⁶, polyvinylchloride, and epoxy resins¹¹⁷, polycarbonate, silicone. Among these, epoxy is the most widely used in electronic package due to its electrical insulation, strong adhesive property, chemical resistance, and strong mechanical strength.

4.2.2 Metals solders and alloy

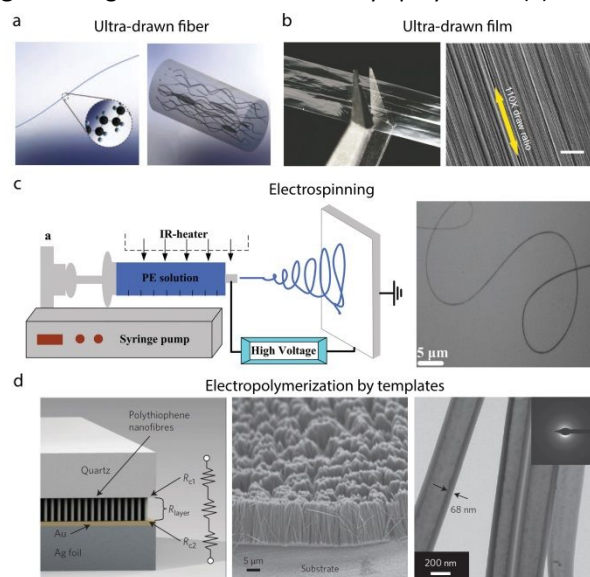
Solder is a fusible metal alloy used to create a permanent bond between metal and workpieces, which is another type of TIMs with the primary aim to reduce TBRs but compromised with the mechanical and electrical requirements¹¹⁸. Due to inherently high thermal conductivity of metals and the reflow process which largely eliminates voids and forms metallurgical bonds, solders can be applied either as solder paste or as a thin foil sheet with or without flux. It provides a continuous metal phase for heat transfer at a high thermal conductivity, eliminating internal interface resistance. However, their rigid structure can lead to poor stress absorption, further leading to cracking during thermal cycling due to coefficient of thermal expansion mismatch. The most common solder to be used in thermal interface applications in industry today is indium¹¹⁹. There are alternatives to solder for metal phase TIMs, such as

Sn–Ag–Cu-based alloys¹²⁰, Sn–Bi alloy¹²¹, sintering Ag nanoparticles/metal composites¹¹⁹.

4.2.3 High thermal conductivity polymers

Despite a poor thermal conductor for typical forms of polymers, recent efforts have shown it may be possible to improve the conductivity via forming high crystalline order and aligning molecular chains^{122–126}. Theoretical predictions based on MD suggest that a very high ($350\text{ W/m}\cdot\text{K}$) or even divergent thermal conductivity can be achieved in an individual polymer (polyethylene) chain¹²⁷. The single polyethylene nanofiber fibre is drawn from the heated gel using either a sharp tungsten tip or a tipless atomic force microscope cantilever. Experimental study on a single polyethylene nanofiber (Figure 11a) shows a high thermal conductivity about $104\text{ W/m}\cdot\text{K}$ ¹²⁴. Other works show that the thermal conductivity of oriented polymer chains can be improved, for example through electro-polymerization¹²⁵, ultra-drawn¹²⁴, electrospinning (Figure 11c)¹²³. For example, Xu et al¹²⁸ report ultra-drawn polyethylene films (Figure 11b) with a high thermal conductivity of $62\text{ W/m}\cdot\text{K}$, over two orders-of-magnitude more conducting than typical polymers ($\sim 0.1\text{ W/m}\cdot\text{K}$). Additional efforts have been made to align polymer chains. For the electro-polymerization, in Figure 11d, Singh et al¹²⁵ utilized electro-polymerization technique in order to achieve the array of polythiophene nanofibres, resulting in the bulk thermal conductivity of $4.4\text{ W/m}\cdot\text{K}$, which is 20 times more than bulk polymer value. The significant molecular chain orientation along the fibre axis is obtained during electro-polymerization using nanoscale templates, which makes this material well-suited for use in TIM applications.

Fig. 11 High thermal conductivity polymers. (a) Vertical



polythiophene nanofibre arrays on a metal substrate by electro-polymerization¹²⁴; Reproduced with permission from ref. 124, copyright 2010 Springer Nature Limited. (b) Photos and SEM image of a thin transparent drawn polyethylene film¹²⁸; Reproduced with permission from ref. 128, copyright 2019 Springer Nature Limited. (c) Electrospinning PE

nanofibers¹²³; Reproduced with permission from ref. 123, copyright 2015 Royal Society of Chemistry. (d) Single molecular chain of polyethylene; bulk polyethylene containing chain ends, entanglements, voids and defects; stretched polyethylene microfibril; TEM image of an ultra-drawn polyethylene nanofibre (from left to right)¹²⁵. Reproduced with permission from ref. 125, copyright 2014 Springer Nature Limited.

4.3 Structural design for TIMs

In addition to materials choice, structural design and optimization is key to improving the thermal performance of TIMs. There are several important structural parameters need to be considered, including filler loading, filler aspect ratio, filler dispersion, filler/polymer interface and alignment of fillers.

For the filler loading, the filler loading can be measured either as weight percentage or volume percentage. Due to the much higher thermal conductivity of fillers compared with pure polymer, a higher filler loading leads to better thermal conductivity of whole composite, but has severe drawbacks both in terms of cost and mechanical properties. Achieving the same great thermal conductive performance but at a lower filler loading would be usually desired in recent research. The filler size and aspect ratio are also an important parameter to affect the thermal conductive performance of filler/polymer TIMs^{129, 130}. The higher aspect ratio of one-dimensional (such as nanowires and nanofibers) or two-dimensional fillers (such as graphene and nanosheet) may be easier in contacting with their neighbors and form a thermal conductive path, however it also introduce anisotropic conductivity^{131, 132}. For the dispersion, a uniform and sufficient dispersion of fillers in matrix is of importance to the thermal performance, however fillers incorporated into polymer matrix tend to agglomerate especially during the curing process. For the filler-matrix interfaces, when fillers are dispersed in a polymer matrix, e.g., epoxy resin, many filler/matrix interfaces would be produced. As discussed in Section 2.1, these interfaces could lead to additional scattering over heat carriers resulting in increased TBR. Surface functionalization can improve the compatibility at the filler-matrix interface, and alignment of fillers can reduce the interface areas, which both will be discussed in the following sections.

4.3.1 Surface functionalization of fillers

The surface chemistry of fillers have been investigated to show importance to improve TIM performance^{10, 112, 133}. Filler surface functionalization to achieve better the compatibility at the interface, for example, through the covalent bonds between the fillers and the matrix, will enable more efficient thermal energy transfer in between and reduce TBR.

Surface functionalization methods can be divided into covalent functionalization, non-covalent functionalization, air plasma functionalization, and low oxide route. Covalent functionalizations is the most common adopted and usually relies on a chemical reaction with a particular functional group. For example, inorganic substances (acids or peroxides¹³⁴), organic acids¹³⁵, isocyanate¹³⁶, phenyletilamine, silane

derivatives¹³⁷ and polysilazane¹³⁸ are common chemicals used to functionalize BN, as showing in Figure 12a. These chemicals are amphiphilic compounds having a group that is compatible with the filler and another group compatible with the matrix, which improve the compatibility at the filler-matrix interface. Non-covalent functionalization (Figure 12c) modifies the interface using π - π interactions, ionic bonding, and hydrogen bonding⁵⁹. The non-covalent functionalization methods are usually easy and reversible because it does not involve the sharing of electrons, but rather involves more dispersed variations of electromagnetic interactions between molecules or within a molecule. The common compounds used to non-covalent functionalized containing alkyl amine, alkyl phosphine, and aromatic groups¹³⁹⁻¹⁴¹. Air plasma treatment is a relatively simple functionalization method requires no chemicals. As showing in Figure 12b, this technique use air flow to allow oxygen to react with water vapor forming ions such as $[H^+]$, $[O_2^-]$, and $[OH^-]$. These ions are very reactive and will attack the filler surface, which control filler wettability and adhesion properties¹⁴². Another approach is via a low oxidation route where fillers at high temperatures in presence of air promote the introduction of oxygen groups onto the filler surface^{143, 144}, as showing in Figure 12d. By treating of fillers at high temperature in air, an oxygen-rich amorphous layer was decorated on fillers. These functionalization can lead to better affinity with matrix and minimize the TBR of TIM.

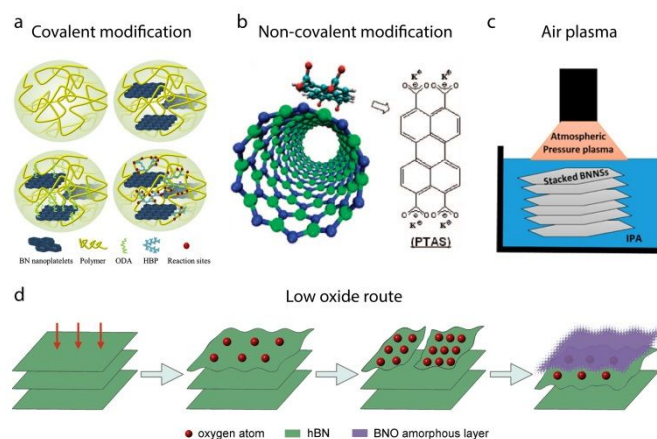


Fig. 12 Surface functionalization of TIM fillers. (a) Covalent functionalization¹⁴⁵, Reproduced with permission from ref. 145, copyright 2012 Elsevier Ltd. (b) Air plasma treatment¹⁴², Reproduced with permission from ref. 142, copyright 2016 American Chemical Society. (c) Non-covalent functionalization¹³⁹, Reproduced with permission from ref. 139, copyright 2008 American Chemical Society. (d) Low oxide route¹⁴⁴. Reproduced with permission from ref. 144, copyright 2016 Elsevier Ltd.

4.3.2 Alignment of fillers

To form good contact network, aligning fillers can form continuous heat conduction pathways and reduce TBR. Many studies have sought to improve TIMs through the distribution of aligned fillers in matrix materials.

Field-driven alignment. One of the most straightforward approaches is to align and form a filler network in a polymer

matrix is through the application of an external field, such as vacuum force^{146, 147}, shear force^{98, 148, 149}, magnetic fields^{150, 151}, electric fields¹⁵²⁻¹⁵⁵, electrostatic flocking¹⁵⁶ and other external fields. For the force field-driven alignment, vacuum-filtration is a route to fabricate composites by assembling the aligned and interconnected fillers in a polymer matrix. During the vacuum filtration process, as showing in Figure 13a, random fillers would be assembly and alignment driven by the vacuum force. For the magnetic field-driven alignment, its advantage is the remote control of filler alignment and possibility of orienting filler at arbitrary directions. A sufficiently high magnetic field is required to reduce the van der Waals forces that attract fillers to each other. As showing in Figure 13b, Wong and Lin et al¹⁵⁰ report magnetic alignment of hexagonal boron nitride (hBN) platelets. The magnetically responsive hBN is produced after surface modification by iron oxide, and their orientations can be controlled by applying an external magnetic field during polymer curing. The magnetic alignment hBN composite exhibits an enhanced thermal conductivity of 0.85 W/m·K, which is 104% higher than that of unaligned counterpart. For the electric field-driven alignment, as showing in Figure 13c¹⁵⁴, the dipole moments are induced when apply a pair of parallel plate electrodes in the electrical fields, causing the filler rotate, orient and move towards the nearest electrode due to the torque force. As a result, the charged fillers are able to migrate and the filler network is stretched across the electrodes to provide a conductivity pathway throughout the sample to facilitate the alignment of fillers within the polymer matrix. For the electrostatic flocking alignment, as showing in Figure 13d¹⁵⁶, vertically aligned, high-density arrays of carbon fibers on a planar substrate by filling the interstitial space of the carbon fibers with elastomeric materials.

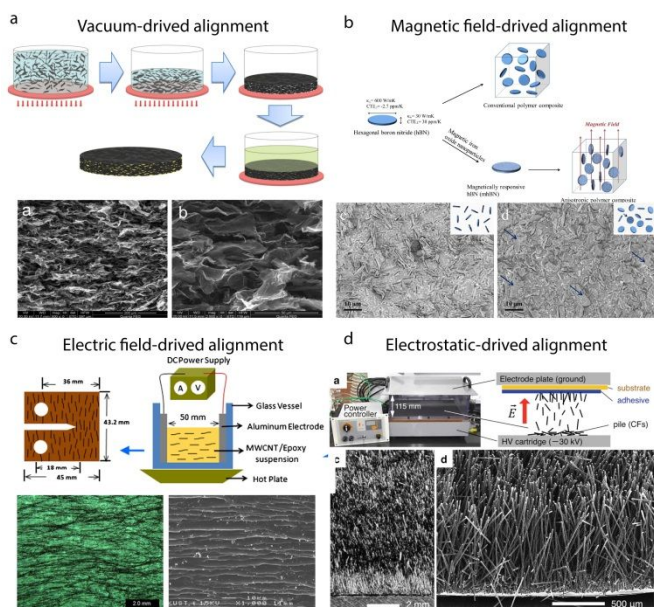


Fig. 13 External field-driven alignment of fillers (a) Vacuum field-driven alignment¹⁴⁶, Reproduced with permission from ref. 146, copyright 2014 American Chemical Society. (b) Magnetic field-driven alignment¹⁵⁰, Reproduced with permission from ref. 150, copyright 2013 American Chemical

Society. (c) Electric field-driven alignment¹⁵⁴, Reproduced with permission from ref. 154, copyright 2013 Elsevier Ltd. (d) Electrostatic-driven alignment¹⁵⁶. Reproduced with permission from ref. 156, copyright 2013 Wiley-VCH.

Templated alignment. Templated assembly has been applied to fabricate well-ordered architectures with various types of materials such as polymers¹⁵⁷, ceramics, and their composites^{98, 157-159}. Figure 14a illustrates the fabrication route for ice-templated alignment⁹⁸. An aqueous suspension was frozen by a directional freezing technique. During freezing process, guided by temperature gradients, ice crystals nucleate and grow into a long-range lamellar pattern along the vertical direction. At the same time, fillers were expelled and assembled to replicate the ice morphology. A filler/polymer composite was then obtained by freeze-drying and subsequent infiltration of a polymer matrix. Yao et al⁹⁸ prepared polymer composites by first constructing stacked boron nitride (BN) platelets reinforced with reduced graphene oxide (rGO) using ice-templated approach and then infiltrating them with epoxy matrix, which exhibit a improved thermal conductivity (5.05 W/m·K) at relatively low loading (13.16 vol%).

Electrospinning alignment. Electrospinning is a widely used industry for fiber production and has been extended to assemble fillers including a wide range of polymer and polymer composites to fabricate nonwoven fibers in the form of membranes, coatings and films within submicron diameters^{123, 160, 161}. Incorporation of nanoscale fillers in electrospun polymeric fibers has been used to increase the functionality of fibers, such as thermal conductivity, mechanical and electrical properties. In a typical Electrospinning process, as illustrated in Figure 14b¹⁶¹, a solution of polymer molecules dissolved in solvent is supplied to the tip of a sharp conductor, such as a syringe needle. A high voltage is applied between the conductor and a grounded collector. Under the influence of the strong electric field, the polymer solution forms a cone (often called a Taylor cone), from which a jet is accelerated towards the grounded collector. This jet is a strong elongational flow, and becomes thinner as it approaches the collector. Due to the very large surface area-to-volume ratio of the jet, the solvent evaporates quickly, leaving a solid fiber that is deposited on the collecting surface.

Chemical growth alignment. Another feasible approach is to align nanostructured fillers directly during materials growth. Individual carbon nanotubes (CNTs) can have thermal conductivities near 3000 W/mK. Vertically aligned CNT films can have axial thermal conductivities as high as those of metals, with reported values reaching ~265 W/mK. For example, as shown in Figure 14c, vertically aligning CNTs has been explored during the chemical vapor deposition^{162, 163} to achieve well aligned bundles. Later on, polymer was infused and aligned interfaces with the axial direction, increasing heat transfer along the CNTs, promises combinations of thermal and mechanical properties. The axial thermal conductivity of the CNT-polymer composites ranges from 0.46 to 4.87 W/mK as the nanotube density increases from 1 vol % to 16.7 vol %.

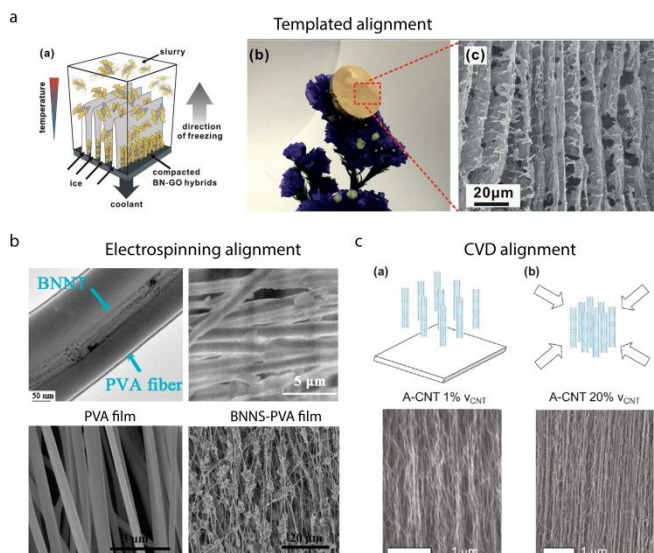


Fig. 14 Alignment of fillers (a) Templated method⁹⁸ Reproduced with permission from ref. 98, copyright 2018 Wiley-VCH. (b) Aligned BNNT-PVA, PVA, and BNNS-PVA film using electrospinning method¹⁶⁴. Reproduced with permission from ref. 164, copyright 2010 American Chemical Society. (c) Aligned CNT film with biaxial mechanically compression up to 20 vol% using chemical vapor deposition (CVD) alignment method⁸³. Reproduced with permission from ref. 83, copyright 2011 American Chemical Society.

5. Summary and outlook

During last decades, tremendous efforts have been devoted to improving the TIMs for electronics thermal management. From a theoretical perspective, recent progress has been developed to better understand the interface energy transport mechanisms and TBRs. Computational approaches to analyze, predict, and optimize TBR will continue to play an important role in developing TIMs. The future theory work may not only aim to elucidate the fundamental limitations of ideal interfaces, but also enable the rational design over practical interfaces with imperfections, as well as the consideration of multi-physical (thermal, mechanical, electrical, optical) properties depending on applications. From an experimental perspective, measurement techniques have been developed to enable reliable thermal characterizations under varied conditions. Experimental efforts have also been devoted to investigating a large range of materials, including the conventional (e.g., BN, Al₂O₃) and carbon-based high thermal conductivity materials (nanotube, graphene/graphite, carbon fibers). Their structural and surface design involving chemistry, physics, and mechanics have been extensively explored to achieve better TIMs. Future opportunities also lie in new building blocks. New semiconductors with ultrahigh thermal conductivity (such as cubic boron arsenide and boron phosphide) are emerging as promising benchmark materials for thermal management. Developing conducting polymers with manufacturing compatibility will lead to significant improvement over conventional matrix materials and new applications. Fundamentally, the understanding of microscopic TBR-

structure relationships is essential to guide rational control over nanostructures and interfaces. Therefore, an interdisciplinary approach that successfully combines experiments and theory, from atomistic, mesoscopic, to macroscopic, is the key to understanding and developing high-performance TIMs.

Conflicts of interest

There are no conflicts to declare.

Acknowledgements

Y. H. acknowledges support from a CAREER award from the National Science Foundation under grant DMR-1753393, an Alfred P. Sloan Research Fellowship under grant FG-2019-11788, a Young Investigator Award from the US Air Force Office of Scientific Research under grant FA9550-17-1-0149, a Doctoral New Investigator Award from the American Chemical Society Petroleum Research Fund under grant 58206-DNI5, the UCLA Sustainable LA Grand Challenge and the Anthony and Jeanne Pritzker Family Foundation.

Notes and references

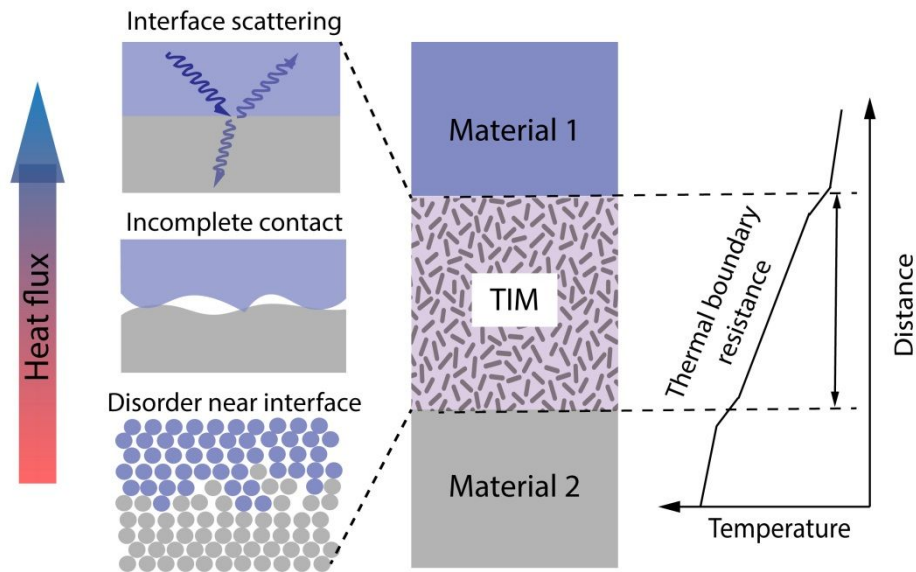
1. *International Technology Roadmap for Semiconductors (ITRS)*, Semiconductor Industry Association, Washington, DC, USA, 2015.
2. P. Ball, *Nature*, 2012, **492**, 174-176.
3. M. M. Waldrop, *Nature* 2016, **530**, 144.
4. S. S. Arman Shehabi, Dale Sartor, Richard Brown, Magnus Herrlin, *United States Data Center Energy Usage Report*, Lawrence Berkeley National Laboratory, 2016.
5. J. S. Kang, M. Li, H. A. Wu, H. Nguyen and Y. J. Hu, *Science*, 2018, **361**, 575-578.
6. J. S. Kang, H. Wu and Y. Hu, *Nano Lett.*, 2017, **17**, 7507-7514.
7. Y. Hu, L. Zeng, A. J. Minnich, M. S. Dresselhaus and G. Chen, *Nat. Nanotechnol.*, 2015, **10**, 701-706.
8. P. W. A. Bar-Cohen, ed., *Nano-Bio-Electronic, Photonic and MemS Packaging*, Springer, New York, 2010.
9. E. Pop, S. Sinha and K. E. Goodson, *Proceedings of the IEEE*, 2006, **94**, 1587-1601.
10. A. J. McNamara, Y. Joshi and Z. M. M. Zhang, *Int J Therm Sci*, 2012, **62**, 2-11.
11. D. G. Cahill, P. V. Braun, G. Chen, D. R. Clarke, S. Fan, K. E. Goodson, P. Keblinski, W. P. King, G. D. Mahan, A. Majumdar, H. J. Maris, S. R. Phillpot, E. Pop and L. Shi, *Appl. Phys. Lett.*, 2014, **1**, 011305.
12. C. Monachon, L. Weber and C. Dames, *Ann. Rev. Mater. Res.*, 2016, **46**, 433-463.
13. M. Li, J. S. Kang, H. D. Nguyen, H. Wu, T. Aoki and Y. Hu, *Adv. Mater.*, 2019, **31**, e1901021.
14. E. T. Swartz and R. O. Pohl, *Rev. Mod. Phys.*, 1989, **61**, 605-668.
15. R. Landauer, *Philos. Mag.*, 2006, **21**, 863-867.
16. R. Landauer, *IBM J. Res. Dev.*, 1957, **1**, 223-231.
17. M. Buttiker, *Phys. Rev. B*, 1988, **38**, 9375-9389.
18. M. Reed, *The quantum hall effect in open conductors. in nanostructured systems*, Semiconductors and Semimetals, Academic, Orlando, 1992.
19. C. W. J. Beenakker and H. v. Houten, *Quantum transport in semiconductor nanostructures*, Solid State Physics, 1991.
20. R. de Picciotto, H. L. Stormer, L. N. Pfeiffer, K. W. Baldwin and K. W. West, *Nature*, 2001, **411**, 51-54.
21. Y. Hu, H. O. Churchill, D. J. Reilly, J. Xiang, C. M. Lieber and C. M. Marcus, *Nat. Nanotechnol.*, 2007, **2**, 622-625.
22. K. G. Rego L G C, *Phys. Rev. Lett.*, 1998, **81**, 232-235.
23. G. Chen, *Nanoscale energy transport and conversion*, Oxford university press, 2005.
24. Z. J. M, *Electrons and phonons: the theory of transport phenomena in solids*, Oxford university press, 2001.
25. P. Reddy, K. Castelino and A. Majumdar, *Appl. Phys. Lett.*, 2005, **87**.

26. Z. Chen, Z. Wei, Y. Chen and C. Dames, *Phys. Rev. B*, 2013, **87**, 125426.
27. M. D. Losego, M. E. Grady, N. R. Sottos, D. G. Cahill and P. V. Braun, *Nat. Mater.*, 2012, **11**, 502-506.
28. W. L. Ong, S. M. Rupich, D. V. Talapin, A. J. McGaughey and J. A. Malen, *Nat. Mater.*, 2013, **12**, 410-415.
29. G. T. Hohensee, R. B. Wilson and D. G. Cahill, *Nat. Commun.*, 2015, **6**, 6578.
30. N. Shenogina, R. Godawat, P. Keblinski and S. Garde, *Phys. Rev. Lett.*, 2009, **102**, 156101.
31. I. M. Khalatnikov, *Zh.Eksp.Teor.Fiz.*, 1952, **22**, 687.
32. B. Auld, *Acoustic fields and waves in solids*, Wiley Press, New York, 1973.
33. M. G. D. Maiti A, Pantelides S T. , *Solid State Commun.*, 1997, **102**, 517-521.
34. E. S. Landry and A. J. H. McGaughey, *Phys. Rev. B*, 2009, **80**, 165304.
35. Y. Chalopin, K. Esfarjani, A. Henry, S. Volz and G. Chen, *Phys. Rev. B*, 2012, **85**, 195302.
36. P. K. Schelling, S. R. Phillpot and P. Keblinski, *J. Appl. Phys.*, 2004, **95**, 6082-6091.
37. D. A. Young and H. J. Maris, *Phys. Rev. B*, 1989, **40**, 3685-3693.
38. S. Pettersson and G. D. Mahan, *Phys. Rev. B*, 1990, **42**, 7386-7390.
39. F. T. S. Zhang W, Mingo N, *J. Heat Transf.*, 2007, **129**, 483-491.
40. Sridhar Sadasivam, Yuhang Che, Zhen Huang, Liang Chen, Satish Kumar and T. S. Fisher, *Annual Rev. Heat Transf.*, 2014, **17**, 89-145.
41. Israelachvili and J. N, *Intermolecular and Surface Forces*, Academic press, 2015.
42. M. S. Daw and M. I. Baskes, *Phys. Rev. B*, 1984, **29**, 6443-6453.
43. F. H. Stillinger and T. A. Weber, *Phys. Rev. B*, 1985, **31**, 5262-5271.
44. J. Tersoff, *Phys. Rev. B*, 1989, **39**, 5566-5568.
45. D. S. Van Duin A C T, Lorant F, *J. Phys. Chem. A*, 2001, **105**, 9396-9409.
46. W. Kohn and L. J. Sham, *Phys. Rev.*, 1965, **140**, A1133-A1138.
47. D. A. Broido, M. Malorny, G. Birner, N. Mingo and D. A. Stewart, *Appl. Phys. Lett.*, 2007, **91**.
48. K. Esfarjani, G. Chen and H. T. Stokes, *Phys. Rev. B*, 2011, **84**, 085204.
49. L. Lindsay, C. Hua, X. L. Ruan and S. Lee, *Mater. Today Phys.*, 2018, **7**, 106-120.
50. H. Fan, H. Wu, L. Lindsay and Y. Hu, *Phys. Rev. B*, 2019, **100**, 085420.
51. D. C. Rapaport and D. C. R. Rapaport, *The art of molecular dynamics simulation*, Cambridge university press, 2004.
52. P. K. Schelling, S. R. Phillpot and P. Keblinski, *Appl. Phys. Lett.*, 2002, **80**, 2484-2486.
53. C. R. Caroli C, Nozieres P, , *J. Phys. C: Solid State Phys.*, 1971, **4**, 916-929.
54. A. International, *Journal*, 2013, **E1225-13** E1225-1213
55. P. Kim, L. Shi, A. Majumdar and P. L. McEuen, *Phys. Rev. Lett.*, 2001, **87**, 215502.
56. L. Shi, D. Y. Li, C. H. Yu, W. Y. Jang, D. Y. Kim, Z. Yao, P. Kim and A. Majumdar, *J. Heat Transf.-Trans. ASME*, 2003, **125**, 1209-1209.
57. J. H. Seol, I. Jo, A. L. Moore, L. Lindsay, Z. H. Aitken, M. T. Pettes, X. S. Li, Z. Yao, R. Huang, D. Broido, N. Mingo, R. S. Ruoff and L. Shi, *Science*, 2010, **328**, 213-216.
58. A. I. Hochbaum, R. Chen, R. D. Delgado, W. Liang, E. C. Garnett, M. Najarian, A. Majumdar and P. Yang, *Nature*, 2008, **451**, 163-167.
59. S. Lee, K. Hippalgaonkar, F. Yang, J. W. Hong, C. Ko, J. Suh, K. Liu, K. Wang, J. Urban, X. Zhang, C. Dames, S. A. Hartnoll, O. Delaire and J. Q. Wu, *Science*, 2017, **355**, 371.
60. J. Yang, Y. Yang, S. W. Waltermire, X. Wu, H. Zhang, T. Gutu, Y. Jiang, Y. Chen, A. A. Zinn, R. Prasher, T. T. Xu and D. Li, *Nat. Nanotechnol.*, 2011, **7**, 91-95.
61. S. Périchon, V. Lysenko, B. Remaki, D. Barbier and B. Champagnon, *J. Appl. Phys.*, 1999, **86**, 4700-4702.
62. D. G. J. J. Healy J J, Kestin J., *Physica B+C*, 1976, **82**, 392-408.
63. M. Li, Z. Qin, Y. Cui, C. Yang, C. Deng, Y. Wang, J. S. Kang, H. Xia and Y. Hu, *Advanced Materials Interfaces*, 2019, **6**.
64. W. J. Parker, R. J. Jenkins, C. P. Butler and G. L. Abbott, *J. Appl. Phys.*, 1961, **32**, 1679-1684.
65. D. G. Cahill, *Rev. Sci. Instrum.*, 1990, **61**, 802-808.
66. Xinwei Wang, Baratunde A. Cola, Thomas L. Bougher, Stephen H. Hodson, Timothy S. Fisher and X. Xu, *Ann. Rev. Mater. Res.*, 2013, **16**, 135-157.
67. B. A. Cola, J. Xu, C. Cheng, X. Xu, T. S. Fisher and H. Hu, *J. Appl. Phys.*, 2007, **101**.
68. A. J. Ångström, *Annalen der Physik und Chemie*, 1861, **114**, 33.
69. Y. Zhu, *Int. J. Heat Mass Transf.*, 2016, **92**, 784-791.
70. Capinski W S and M. H. J, *Physica B* 1996, **219**, 699-701.
71. D. G. Cahill, *Rev. Sci. Instrum.*, 2004, **75**, 5119-5122.
72. A. J. Schmidt, X. Chen and G. Chen, *Rev. Sci. Instrum.*, 2008, **79**, 114902.
73. A. J. Schmidt, R. Cheaito and M. Chiesa, *Rev. Sci. Instrum.*, 2009, **80**, 094901.
74. J. A. Rogers, A. A. Maznev, M. J. Banet and K. A. Nelson, *Annu. Rev. Mater. Sci.*, 2000, **30**, 117-157.
75. Y. Yan, S. C. King, M. Li, T. Galy, M. Marszewski, J. S. Kang, L. Pilon, Y. Hu and S. H. Tolbert, *J Phys Chem C*, 2019, **123**, 21721-21730.
76. J. S. Kang, M. Ke and Y. Hu, *Nano Lett.*, 2017, **17**, 1431-1438.
77. J. S. Kang, H. Wu, M. Li and Y. Hu, *Nano Lett.*, 2019, **19**, 4941-4948.
78. M. Li, J. S. Kang and Y. Hu, *Rev. Sci. Instrum.*, 2018, **89**, 084901.
79. N. A. Rongione, M. Li, H. Wu, H. D. Nguyen, J. S. Kang, B. Ouyang, H. Xia and Y. Hu, *Adv. Electron. Mater.*, 2019, **5**.
80. V. Mishra, C. L. Hardin, J. E. Garay and C. Dames, *Rev. Sci. Instrum.*, 2015, **86**, 054902.
81. Y. Yao, X. Zeng, K. Guo, R. Sun and J.-b. Xu, *Compos. Pt. A- Appl. Sci. Manuf.*, 2015, **69**, 49-55.
82. J. Chen, X. Huang, Y. Zhu and P. Jiang, *Adv. Funct. Mater.*, 2017, **27**.
83. A. M. Marconnett, N. Yamamoto, M. A. Panzer, B. L. Wardle and K. E. Goodson, *ACS Nano*, 2011, **5**, 4818-4825.
84. Y. S. Song and J. R. Youn, *Carbon*, 2005, **43**, 1378-1385.
85. L. M. Veca, M. J. Mezzani, W. Wang, X. Wang, F. Lu, P. Zhang, Y. Lin, R. Fee, J. W. Connell and Y.-P. Sun, *Adv. Mater.*, 2009, **21**, 2088-2092.
86. H. Wang, A. S. Tazebay, G. Yang, H. T. Lin, W. Choi and C. Yu, *Carbon*, 2016, **106**, 152-157.
87. S. Wang, Y. Cheng, R. Wang, J. Sun and L. Gao, *ACS Appl. Mater. Interfaces*, 2014, **6**, 6481-6486.
88. C. H. Yu, L. Shi, Z. Yao, D. Y. Li and A. Majumdar, *Nano Lett.*, 2005, **5**, 1842-1846.
89. J. S. Kang, M. Li, H. Wu, H. Nguyen and Y. Hu, *Appl. Phys. Lett.*, 2019, **115**, 122103.
90. C. F. Deng, Y. X. Ma, P. Zhang, X. X. Zhang and D. Z. Wang, *Mater. Lett.*, 2008, **62**, 2301-2303.
91. K. Pashayi, H. R. Fard, F. Lai, S. Iruvanti, J. Plawsky and T. Borca-Tasciuc, *Nanoscale*, 2014, **6**, 4292-4296.
92. D. Kuang, L. Xu, L. Liu, W. Hu and Y. Wu, *Appl. Surf. Sci.*, 2013, **273**, 484-490.
93. J. Hansson, T. M. J. Nilsson, L. Ye and J. Liu, *Int. Mater. Rev.*, 2017, **63**, 22-45.
94. L. Chen, Y.-Y. Sun, J. Lin, X.-Z. Du, G.-S. Wei, S.-J. He and S. Nazarenko, *Int. J. Heat Mass Transf.*, 2015, **81**, 457-464.
95. M. A. Raza, A. V. K. Westwood, C. Stirling and R. Ahmad, *Compos. Sci. Technol.*, 2015, **120**, 9-16.
96. H. Im and J. Kim, *Carbon*, 2012, **50**, 5429-5440.
97. K. M. Shahil and A. A. Balandin, *Nano Lett.*, 2012, **12**, 861-867.
98. Y. Yao, J. Sun, X. Zeng, R. Sun, J. B. Xu and C. P. Wong, *Small*, 2018, **14**, e1704044.
99. F. Yang and C. Dames, *Phys. Rev. B*, 2013, **87**, 035437
100. C. Dames and G. Chen, *Thermoelectrics handbook, macro to nano*, CRC Press, 2006.
101. L. Lindsay, W. Li, J. Carrete, N. Mingo, D. A. Broido and T. L. Reinecke, *Phys. Rev. B*, 2014, **89**, 155426.
102. W. Yu, H. Xie, L. Yin, J. Zhao, L. Xia and L. Chen, *Int. J. Therm. Sci.*, 2015, **91**, 76-82.
103. M. G. Holland, *Phys. Rev.*, 1964, **134**, A471-A480.
104. A. A. Balandin, *Nat Mater*, 2011, **10**, 569-581.
105. S. Stankovich, D. A. Dikin, G. H. Dommett, K. M. Kohlhaas, E. J. Zimney, E. A. Stach, R. D. Piner, S. T. Nguyen and R. S. Ruoff, *Nature*, 2006, **442**, 282-286.
106. L. Lindsay, D. A. Broido and T. L. Reinecke, *Phys. Rev. Lett.*, 2013, **111**, 025901.
107. T. Feng, L. Lindsay and X. Ruan, *Phys. Rev. B*, 2017, **96**, 161201.
108. H. Fan, H. Wu, L. Lindsay and Y. Hu, *Phys. Rev. B*, 2019, **100**, 085420.
109. F. Tian, B. Song, X. Chen, N. K. Ravichandran, Y. C. Lv, K. Chen, S. Sullivan, J. Kim, Y. Y. Zhou, T. H. Liu, M. Goni, Z. W. Ding, J. Y. Sun, G. A. G. U. Gamage, H. R. Sun, H. Ziyadee, S. Y. Huyan, L. Z. Deng, J. S. Zhou, A. J. Schmidt, S. Chen, C. W. Chu, P. S. E. Y. Huang, D. Broido, L. Shi, G. Chen and Z. F. Ren, *Science*, 2018, **361**, 582-585.
110. S. Li, Q. Y. Zheng, Y. C. Lv, X. Y. Liu, X. Q. Wang, P. S. E. Y. Huang, D. G. Cahill and B. Lv, *Science*, 2018, **361**, 579-581.
111. V. Subramanian, J. Sanchez, J. Bautista, Y. He, J. Wang, A. Das, J. G. R. Schuldes, K. Yazzie, H. K. Dhavaleswarapu and P. Malatkar, *J Electron Packaging*, 2019, **141**, 010804.
112. H. S. Kim, J.-u. Jang, H. Lee, S. Y. Kim, S. H. Kim, J. Kim, Y. C. Jung and B. J. Yang, *Adv. Eng. Mater.*, 2018, **20**, 1800204.
113. M. A. Vadivelu, C. R. Kumar and G. M. Joshi, *Compos. Interfaces*, 2016, **23**, 847-872.
114. D. Kumlutas, I. H. Tavman and M. T. Coban, *Compos. Sci. Technol.*, 2003, **63**, 113-117.
115. A. Boudenne, L. Ibos, M. Fois, J. C. Majesté and E. Géhin, *Compos. Pt. A- Appl. Sci. Manuf.*, 2005, **36**, 1545-1554.
116. H. S. Tekce, D. Kumlutas and I. H. Tavman, *J. Reinf. Plast. Compos.*, 2016, **26**, 113-121.
117. Y. P. Mamunya, V. V. Davydenko, P. Pissis and E. Lebedev, *Eur. Polym. J.*, 2002, **38**, 1887-1897.
118. T. E. Graedel, E. M. Harper, N. T. Nassar, P. Nuss and B. K. Reck, *Proc. Natl. Acad. Sci. U. S. A.*, 2015, **112**, 4257-4262.
119. I. Dutta, R. Raj, P. Kumar, T. Chen, C. M. Nagaraj, J. Liu, M. Renavikar and V. Wakharkar, *J. Electron. Mater.*, 2009, **38**, 2735-2745.
120. M. Ekpou, R. Bhatti, M. I. Okereke, S. Mallik and K. Otiaba, *Microelectron. Reliab.*, 2014, **54**, 239-244.

121. R. Zhang, J. Cai, Q. Wang, J. Li, Y. Hu, H. Du and L. Li, *J. Electron. Packag.*, 2014, **136**, 011012.
122. G. H. Kim, D. Lee, A. Shanker, L. Shao, M. S. Kwon, D. Gidley, J. Kim and K. P. Pipe, *Nat. Mater.*, 2015, **14**, 295-300.
123. J. Ma, Q. Zhang, A. Mayo, Z. Ni, H. Yi, Y. Chen, R. Mu, L. M. Bellan and D. Li, *Nanoscale*, 2015, **7**, 16899-16908.
124. S. Shen, A. Henry, J. Tong, R. Zheng and G. Chen, *Nat. Nanotechnol.*, 2010, **5**, 251-255.
125. V. Singh, T. L. Bougher, A. Weathers, Y. Cai, K. Bi, M. T. Pettes, S. A. McMamin, W. Lv, D. P. Resler, T. R. Gattuso, D. H. Altman, K. H. Sandhage, L. Shi, A. Henry and B. A. Cola, *Nat. Nanotechnol.*, 2014, **9**, 384-390.
126. Y. F. Xu, X. X. Wang, J. W. Zhou, B. Song, Z. Jiang, E. M. Y. Lee, S. Huberman, K. K. Gleason and G. Chen, *Sci. Adv.*, 2018, **4**, eaar3031.
127. A. Henry and G. Chen, *Phys. Rev. Lett.*, 2008, **101**, 235502.
128. Y. Xu, D. Kraemer, B. Song, Z. Jiang, J. Zhou, J. Loomis, J. Wang, M. Li, H. Ghaseemi, X. Huang, X. Li and G. Chen, *Nat. Commun.*, 2019, **10**, 1771.
129. J. Li, P. C. Ma, W. S. Chow, C. K. To, B. Z. Tang and J. K. Kim, *Adv. Funct. Mater.*, 2007, **17**, 3207-3215.
130. F. Deng, Q.-S. Zheng, L.-F. Wang and C.-W. Nan, *Applied Physics Letters*, 2007, **90**.
131. J.-F. Su, Y.-H. Zhao, X.-Y. Wang, H. Dong and S.-B. Wang, *Compos. Pt. A- Appl. Sci. Manuf.*, 2012, **43**, 325-332.
132. B. L. Zhu, J. Wang, H. Zheng, J. Ma, J. Wu and R. Wu, *Compos. Pt. B-Eng.*, 2015, **69**, 496-506.
133. A. Bar-Cohen, K. Matin and S. Narumanchi, *J. Electron. Packag.*, 2015, **137**, 040803.
134. J. Hou, G. Li, N. Yang, L. Qin, M. E. Grami, Q. Zhang, N. Wang and X. Qu, *RSC Adv.*, 2014, **4**, 44282-44290.
135. D. Lee, S. H. Song, J. Hwang, S. H. Jin, K. H. Park, B. H. Kim, S. H. Hong and S. Jeon, *Small*, 2013, **9**, 2602-2610.
136. W. Jin, W. Zhang, Y. Gao, G. Liang, A. Gu and L. Yuan, *Appl. Surf. Sci.*, 2013, **270**, 561-571.
137. Y. Xu and D. D. L. Chung, *Compos. Interfaces*, 2012, **7**, 243-256.
138. K. Ahn, K. Kim, M. Kim and J. Kim, *Ceram. Int.*, 2015, **41**, 2187-2195.
139. W. L. Wang, Y. Bando, C. Y. Zhi, W. Y. Fu, E. G. Wang and D. Golberg, *J. Am. Chem. Soc.*, 2008, **130**, 8144-8145.
140. C. Zhi, Y. Bando, C. Tang and D. Golberg, *J. Am. Chem. Soc.*, 2005, **127**, 17144-17145.
141. C. Y. Zhi, Y. Bando, C. C. Tang, R. G. Xie, T. Sekiguchi and D. Golberg, *J. Am. Chem. Soc.*, 2005, **127**, 15996-15997.
142. R. C. Zhang, D. Sun, A. Lu, S. Askari, M. Macias-Montero, P. Joseph, D. Dixon, K. Ostrikov, P. Maguire and D. Mariotti, *ACS Appl. Mater. Interfaces*, 2016, **8**, 13567-13572.
143. T. Sainsbury, A. Satti, P. May, Z. Wang, I. McGovern, Y. K. Gun'ko and J. Coleman, *J. Am. Chem. Soc.*, 2012, **134**, 18758-18771.
144. H. Jin, Y. Li, X. Li, Z. Shi, H. Xia, Z. Xu and G. Qiao, *Mater. Lett.*, 2016, **175**, 244-247.
145. J. Yu, X. Huang, C. Wu, X. Wu, G. Wang and P. Jiang, *Polymer*, 2012, **53**, 471-480.
146. Q. Li, Y. Guo, W. Li, S. Qiu, C. Zhu, X. Wei, M. Chen, C. Liu, S. Liao, Y. Gong, A. K. Mishra and L. Liu, *Chem. Mat.*, 2014, **26**, 4459-4465.
147. X. Zeng, J. Sun, Y. Yao, R. Sun, J. B. Xu and C. P. Wong, *ACS Nano*, 2017, **11**, 5167-5178.
148. H. Jung, S. Yu, N. S. Bae, S. M. Cho, R. H. Kim, S. H. Cho, I. Hwang, B. Jeong, J. S. Ryu, J. Hwang, S. M. Hong, C. M. Koo and C. Park, *ACS Appl. Mater. Interfaces*, 2015, **7**, 15256-15262.
149. Z. Kuang, Y. Chen, Y. Lu, L. Liu, S. Hu, S. Wen, Y. Mao and L. Zhang, *Small*, 2015, **11**, 1655-1659.
150. Z. Lin, Y. Liu, S. Raghavan, K. S. Moon, S. K. Sitaraman and C. P. Wong, *ACS Appl. Mater. Interfaces*, 2013, **5**, 7633-7640.
151. A. Sharma, B. Tripathi and Y. K. Vijay, *J. Membr. Sci.*, 2010, **361**, 89-95.
152. H.-B. Cho, A. Konno, T. Fujihara, T. Suzuki, S. Tanaka, W. Jiang, H. Suematsu, K. Niihara and T. Nakayama, *Compos. Sci. Technol.*, 2011, **72**, 112-118.
153. P. V. Kamat, K. G. Thomas, S. Barazzouk, G. Girishkumar, K. Vinodgopal and D. Meisel, *J. Am. Chem. Soc.*, 2004, **126**, 10757-10762.
154. S. U. Khan, J. R. Pothnis and J.-K. Kim, *Compos. Pt. A- Appl. Sci. Manuf.*, 2013, **49**, 26-34.
155. C. A. Martin, J. K. W. Sandler, A. H. Windle, M. K. Schwarz, W. Bauhofer, K. Schulte and M. S. P. Shaffer, *Polymer*, 2005, **46**, 877-886.
156. K. Uetani, S. Ata, S. Tomonoh, T. Yamada, M. Yumura and K. Hata, *Adv. Mater.*, 2014, **26**, 5857-5862.
157. H. Zhang, I. Hussain, M. Brust, M. F. Butler, S. P. Rannard and A. I. Cooper, *Nat. Mater.*, 2005, **4**, 787-793.
158. J. Han, G. Du, W. Gao and H. Bai, *Adv. Funct. Mater.*, 2019, **29**, 1900412.
159. X. Zeng, Y. Yao, Z. Gong, F. Wang, R. Sun, J. Xu and C. P. Wong, *Small*, 2015, **11**, 6205-6213.
160. J. Chen, X. Huang, B. Sun, Y. Wang, Y. Zhu and P. Jiang, *ACS Appl. Mater. Interfaces*, 2017, **9**, 30909-30917.
161. T. Terao, C. Y. Zhi, Y. Bando, M. Mitome, C. C. Tang and D. Golberg, *J. Phys. Chem. C*, 2010, **114**, 4340-4344.
162. S. Kaur, N. Raravikar, B. A. Helms, R. Prasher and D. F. Ogletree, *Nat. Commun.*, 2014, **5**, 3082.
163. M. A. Panzer, H. M. Duong, J. Okawa, J. Shiomi, B. L. Wardle, S. Maruyama and K. E. Goodson, *Nano Lett.*, 2010, **10**, 2395-2400.
164. T. Terao, C. Y. Zhi, Y. Bando, M. Mitome, C. C. Tang and D. Golberg, *J. Phys. Chem. C*, 2010, **114**, 4340-4344.

Table of contents entry

Graphic:



One sentence of text:

State-of-the-art experiments and modeling, challenges, and future opportunities to develop high-performance interface materials for electronics thermal management.